Clinical & Translational Immunology

Australian and New Zealand Society for Immunology Inc.

Clinical & Translational Immunology 2021; e1252. doi: 10.1002/cti2.1252
www.wileyonlinelibrary.com/journal/cti

ORIGINAL ARTICLE

Tumor-associated neutrophils (TANs) in human carcinoma-draining lymph nodes: a novel TAN compartment

Silvia Lonardi[1,2,†], Francesco Missale[3,4,†], Stefano Calza[5,6,7], Mattia Bugatti[1,2], Raffaella Vescovi[1], Bresciani Debora[1,2], Ravindra Uppaluri[8], Ann Marie Egloff[8], Davide Mattavelli[3], Davide Lombardi[2,3], Luisa Benerini Gatta[1,2], Olivia Marini[9], Nicola Tamassia[9], Elisa Gardiman[9], Marco A Cassatella[9], Patrizia Scapini[9], Piero Nicolai[2,3] & William Vermi[1,2,10]

[1]Section of Pathology, Department of Molecular and Translational Medicine, University of Brescia, Brescia, Italy
[2]ASST- Spedali Civili di Brescia, Brescia, Italy
[3]Unit of Otorhinolaryngology - Head and Neck Surgery, Department of Surgical Specialties, Radiological Sciences, and Public Health, University of Brescia, Brescia, Italy
[4]IRCCS Ospedale Policlinico San Martino, Unit of Otorhinolaryngology, Head and Neck Surgery, Department of Surgical and Diagnostic Integrated Sciences, University of Genoa, Genoa, Italy
[5]Unit of Biostatistics, Department of Molecular and Translational Medicine, University of Brescia, Brescia, Italy
[6]Department of Medical Epidemiology and Biostatistics, Karolinska Institutet, Stockholm, Sweden
[7]Big&Open Data Innovation Laboratory, University of Brescia, Brescia, Italy
[8]Department of Surgery/Otolaryngology, Brigham and Women's Hospital and Dana-Farber Cancer Institute and Harvard Medical School, Boston, MA, USA
[9]Section of General Pathology, Department of Medicine, University of Verona, Verona, Italy
[10]Department of Pathology and Immunology, Washington University, Saint Louis, MO, USA

Correspondence
W Vermi, Department of Molecular and Translational Medicine, Section of Pathology, P.le Spedali Civili 1, 25123 Brescia, Italy.
E-mail: william.vermi@unibs.it

[†]Equal contributors.

Received 28 August 2020;
Revised 4 December 2020
and 19 January 2021;
Accepted 19 January 2021

doi: 10.1002/cti2.1252

Clinical & Translational Immunology
2021; **10**: e1252

Abstract

Objectives. The role of tumor-associated neutrophils (TANs) in the nodal spread of cancer cells remains unexplored. The present study evaluates the occurrence and clinical significance of human nodal TANs. **Methods.** The relevance, derivation, phenotype and interactions of nodal TANs were explored *via* a large immunohistochemical analysis of carcinoma-draining lymph nodes, and their clinical significance was evaluated on a retrospective cohort of oral squamous cell carcinomas (OSCC). The tumor-promoting function of nodal TAN was probed in the OSCC TCGA dataset combining TAN and epithelial-to-mesenchymal transition (EMT) signatures. **Results.** The pan-carcinoma screening identified a consistent infiltration (59%) of CD66b^{+} TANs in tumor-draining lymph nodes (TDLNs). Microscopic findings, including the occurrence of intra-lymphatic conjugates of TANs and cancer cells, indicate that TANs migrate through lymphatic vessels. *In vitro* experiments revealed that OSCC cell lines sustain neutrophil viability and activation via release of GM-CSF. Moreover, by retrospective analysis, a high CD66b^{+} TAN density in M-TDLNs of OSCC (n = 182 patients) predicted a worse prognosis. The analysis of the OSCC-TCGA dataset unveiled that the expression of a set of neutrophil-specific genes in the primary tumor (PT) is highly associated with an EMT signature, which predicts nodal spread. Accordingly, in the PT of OSCC cases, CD66b^{+}TANs co-localised with PDPN^{+}S100A9^{-} EMT-switched tumor cells in areas of

lymphangiogenesis. The pro-EMT signature is lacking in peripheral blood neutrophils from OSCC patients, suggesting tissue skewing of TANs. **Conclusion.** Our findings are consistent with a novel pro-tumoral TAN compartment that may promote nodal spread *via* EMT, through the lymphatics.

Keywords: carcinoma, epithelial-to-mesenchymal transition, lymph nodes, metastasis, tumor-associated neutrophils

INTRODUCTION

Tumor-associated myeloid cells encompass a large variety of circulating and tissue cellular components at various stages of differentiation. Among them, tumor-associated macrophages, dendritic cells and neutrophils represent the most well-characterised cell populations.[1–3] As a group, tumor-associated myeloid cells exert pro-tumor functions, but recent data have challenged this view, suggesting an extreme plasticity of these cells modulated by the tumor microenvironment at various disease stages.[4]

Emergency granulopoiesis[5] is prominent in late-stage cancer and mostly accounts for the high neutrophil count and the altered neutrophil-to-lymphocyte ratio (NLR) in advanced stages. Within the expanded granulocyte compartment, various subpopulations have been identified based on their ontogeny, fraction in the density gradient separation, phenotype and function.[5–7] Among the circulating neutrophils, immunosuppressive low-density neutrophils (LDNs), known as polymorphonuclear myeloid-derived suppressor cells (PMN-MDSCs), have recently gained great attention.[7] An additional granulocyte population is represented by neutrophils found within the tumor tissues, the so-called tumor-associated neutrophils (TANs).[8] Their connection with LDNs/PMN-MDSCs and normal circulating neutrophils still remains unclear due to the lack of specific markers. Similarly to tumor-associated macrophages,[2] TANs can be polarised *in vitro*.[9,10] N1-type TANs, induced by type I IFN, mainly exert anti-tumoral functions[10] and promote cancer cell elimination. On the contrary, N2-type TANs are TGF-β-driven and sustain tumor cell proliferation, angiogenesis, invasion, metastasis and immune escape.[8,9,11] Data on TAN polarisation are limited to murine models, and it is still unknown whether human TANs display similar polarisation. Most of the studies performed in retrospective cancer cohorts[12] have supported a pro-tumor function of TANs, with a high TAN tumor density significantly associated with a worse outcome.[13] Although this finding supports a dominant N2 polarisation of TANs in human cancer, emerging data have revealed extreme plasticity of these cells. Specifically, when purified from early-stage cancers, TANs exert anti-tumor activities and display a hybrid phenotype together with antigen-presenting cell features.[14,15]

Data on the biological and clinical significance of TANs have been obtained with the leading assumption that they execute their programs at the primary tumor (PT) site or in distant metastasis and largely ignoring their role in the tumor-draining lymph nodes (TDLNs). Nodal colonisation by cancer cells is a harbinger of systemic tumor spread and this is clinically relevant in a significant fraction of cancer types.[16] In addition, TDLNs are crucial sites for the organisation of the immune response to tumor antigens. A significant component of the tumor-promoting activity of LDNs/PMN-MDSCs and TANs derives from their negative modulation of the anti-tumor T-cell response.[5,7,8] Recent studies in mouse models have shown that neutrophil entry into the node results in a potent negative regulation of the specific T-cell response to pathogens.[17–19] However, very limited data are available on the identification of nodal TANs and their characterisation during cancer evolution in humans.

Herein, by performing a screening of human cancer tissues including PTs and TDLNs, we identified that high $CD66b^+$ TAN density is common in TDLNs from various primary sites. $CD66b^+$ TANs in TDLNs co-express classical neutrophil markers, as well as the recently identified markers of PMN-MDSCs such as S100A9,[20] arginase-1, pSTAT3 and c/EBPβ.[21] Our data support the notion that TANs could enter the TDLN via lymphatic vessels, forming intraluminal conjugates with cancer cells. The preferential TAN interplay with cancer cells has

recently been reported including in squamous cell carcinomas (SCC).[22–25] By the analysis of a retrospective cohort, colonisation of carcinoma-draining lymph nodes by TANs predicts poor outcome in advanced oral squamous cell cancer (OSCC). Accordingly, increased CD66b$^+$ TAN density correlated with recurrent head and neck SCC. By *in silico* evaluation of the OSCC TCGA dataset, we found that expression of a set of neutrophil-specific genes at the PT is associated with an epithelial-to-mesenchymal transition (EMT) signature, the latter known to predict nodal spread in OSCC.[26] These findings highlight a hitherto unrecognised contribution of TANs in nodal colonisation by modulating EMT-dependent lymphatic spread.

RESULTS

CD66b$^+$ TANs recurrently accumulate in carcinoma-draining lymph nodes

A large number of studies have documented the clinical relevance of TANs infiltrating the primary tumor (PT) site and distant metastasis.[9,13] We recently observed that CD66b$^+$ TANs are also found in metastatic tumor-draining lymph nodes (M-TDLNs) from patients with colon carcinomas.[27] To further follow up this finding, we extended our characterisation to a larger cohort of cancer patients. Compared to other myeloid markers, CD66b is selectively expressed by granulocytes. Clone G10F5 is suitable for staining on FFPE sections and, among immune cells, it is selectively restricted to mature neutrophils, as demonstrated by the analysis of primary (n = 6) and secondary (n = 30) lymphoid organs (Supplementary figure 1a–h). In inflamed lymph nodes from non-tumor-bearing hosts (n = 21), CD66b$^+$ neutrophils are generally scant and limited to the HEV dilated lumen (Supplementary figure 1e) with the exception of suppurative necrotising lymphadenitis of infectious origin (n = 3; Supplementary figure 1f). By using archival material, we analysed a total of 278 M-TDLNs of carcinomas from various primary sites (Supplementary table 1). Nodal localisation of CD66b$^+$ TANs was observed in 59% of M-TDLNs (n = 165/278). Based on a three-tiered scoring system (score 0, 1 and 2; illustrated in Supplementary figure 2 and detailed in the Methods), CD66b$^+$ TAN infiltration was highly dense (score 2) in 31.5% of the M-TDLNs (n = 52/165) from various primary sites and with different histologies (Figure 1a, Supplementary figure 2 and Supplementary table 1). Dense CD66b$^+$ TAN infiltration was common in head and neck squamous cell carcinomas, adenocarcinomas of the gastrointestinal tract, of the pancreas, of the thyroid and ovary, as well as in urothelial bladder cancer. On the contrary, CD66b$^+$ TANs were rarely observed in breast carcinoma (Supplementary table 1 and Figure 1a). We extended the latter finding on breast carcinoma to an additional cohort (n = 38) and compared concurrently removed M-TDLNs and PT (n = 22). A low CD66b$^+$ TAN density was confirmed in the majority of the cases including in the PTs (Supplementary figure 2i, j).

In term of nodal localisation (Figure 1b–f and Supplementary figure 3), CD66b$^+$ TANs in M-TDLNs were localised within and immediately around the metastatic deposits (M-TDLN^M) (n = 100/165; 60.6% $CI_{95\%}$ 52.7–68.1%) (Figure 1b and d green asterisks). They were also present in the remaining spared nodal parenchyma (M-TDLN^P), where they were located mainly within the lumen of marginal, intermediate and medullary lymphatic sinuses (n = 90/165; 54.5% $CI_{95\%}$ 46.6–62.3%; Figure 1b, c and e red asterisks). The identity of the expanded lymphatic sinuses was confirmed by using a set of endothelial cell markers including podoplanin, CD31, Lyve-1, CD34, ERG, Factor VIII, and CLA/HECA 452 (Figure 1f, Supplementary figure 4a–e) in M-TDLNs cases (n = 10). CD66b$^+$ TANs frequently engulfed some dilated HEVs (Supplementary figure 4f). However, as evaluated by double immunohistochemistry, CD66b$^+$ TANs were only rarely observed as transmigrating cells (Supplementary figure 4g) or closely surrounding HEV (n = 10).

The expression of a panel of neutrophil-specific molecules suitable for archival tissue was analysed in a set of M-TDLNs and matched PTs (n = 9). CD66b$^+$ TANs showed a segmented nucleus and co-expressed CD11b, CD10, CD16, myeloperoxidase, neutrophil elastase and cytoplasmic granule-associated molecules confirming their neutrophil identity and mature phenotype (Supplementary figure 5a–j).

CD66b$^+$ TANs engulf lymphatic vessels of the PTs and predict the TDLN colonisation of cancer cells

Recently, by using murine models, a number of studies have shown that neutrophils can also

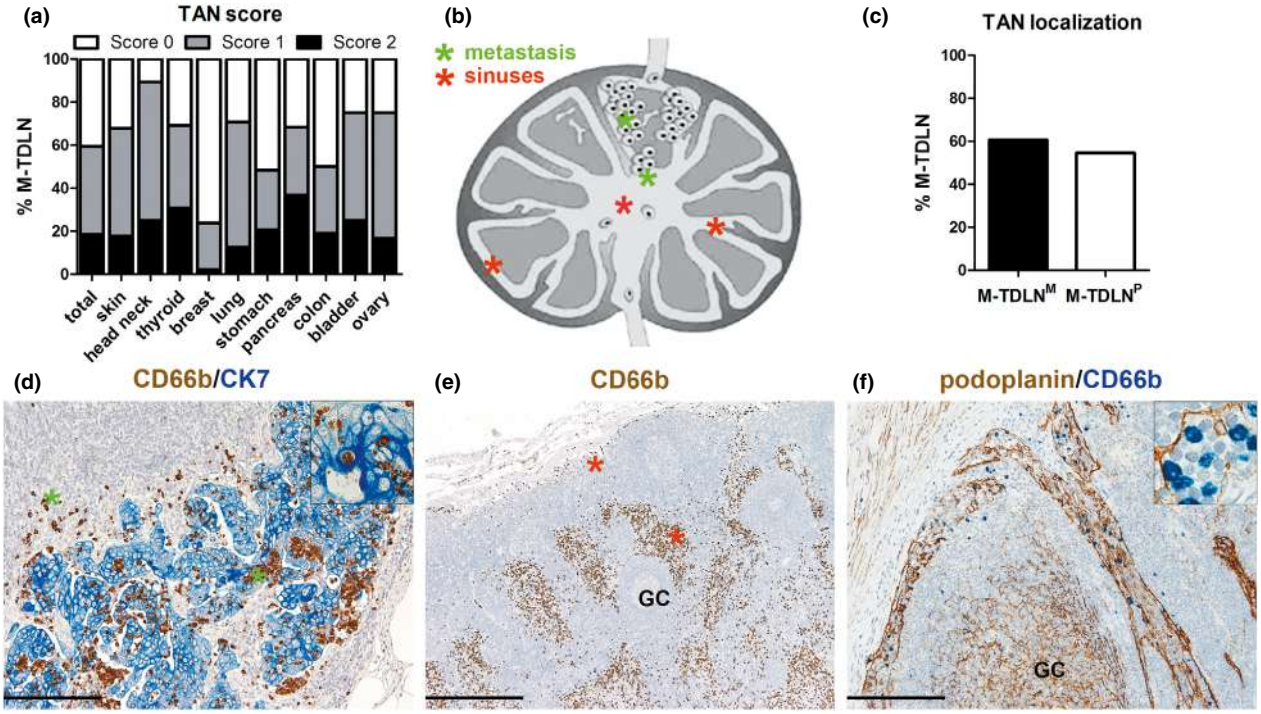

Figure 1. CD66b$^+$ TAN density and localisation in M-TDLN. **(a)** The density of CD66b$^+$ TANs expressed as TAN score (S0 = white, S1 = grey, S2 = black; three-tiered score is reported in the Methods section) in 278 M-TDLNs obtained from various primary carcinomas. **(b)** The distribution of CD66b$^+$ TANs in different LN compartments (red asterisks indicate marginal, intermediate sinuses and medullary sinuses whereas green asterisks indicate CD66b$^+$ cells within and around the metastatic nest). **(c)** The density of CD66b$^+$ TANs localised in the metastatic nest (M-TDLN^M, black column) and in the surrounding nodal parenchyma (M-TDLN^P, white column). Sections are from cases of M-TDLN of colon carcinoma **(d)** and head and neck squamous cell carcinoma **(e, f)**, stained as labelled (CK = cytokeratin 7) and illustrating CD66b$^+$ TANs within and around (**d,** green asterisks) the metastatic nests, within marginal and intermediate sinuses (**e**, red asterisk and **f**). In **f**, lymphatic sinuses are identified by positivity for podoplanin. Sections are counterstained with haematoxylin. Original magnification: 40× (**e**, scale bar 500 μm), 100× (**d**, **f**, scale bar 200 μm), 400× (inset in **d**), 600× (inset in **f**). GC, germinal centre.

traffic through the lymph in response to pathogens,[17,18,28] raising the possibility that neutrophils modulate adaptive immunity directly within the lymph node.[29] Our data on the localisation of CD66b$^+$ TANs in nodal sinuses of TDLNs strongly support their migration from the primary tumor site through the lymphatic system. This hypothesis is further strengthened by a set of indirect findings. First, CD66b$^+$ TANs from M-TDLNs are negative for active caspase-3 (n = 10) and ki-67 (Figure 2a–d) (n = 13), indicating that the CD66b$^+$TAN pool is less susceptible to spontaneous apoptosis and independent from local self-renewal, as other tumor-associated innate components.[30] Moreover, by comparative analysis of PTs and matched M-TDLNs (n = 45), we found a high correlation (Spearman r = 0.77; P < 0.0001) between CD66b$^+$ TAN density scores (Supplementary figure 2g–l). Finally, as observed by double immunohistochemistry on serial sections of M-TDLNs (n = 4), CD66b$^+$ TANs in the PTs were often detected within enlarged lymphatic vessels in the form of multicellular tumor emboli admixed with carcinoma cells (Figure 2e and f), T cells (Figure 2g) and macrophages (Figure 2h). Remarkably, this multicellular interaction was not limited to the PT lymphatic vessels, but was also detectable within the marginal sinuses of M-TDLNs (Figure 2i; n = 5). TAN migration *via* lymphatics requires endothelial activation for adhesion, integrin-mediated binding through ICAM-1 and VCAM-1 and CXCL8-dependent chemotaxis.[31–33] We found that CXCL8 is expressed in PT cases (n = 5) with massive CD66b$^+$ TAN embolisation (Figure 2j and k), with the main cellular source represented by the CD66b$^+$ TANs themselves (Figure 2j and inset); CXCL8$^+$CD66b$^+$ TANs were also detected in lymphatic sinuses of M-TDLNs (Figure 2l). Since TANs and tumor cells share their path to TDLNs, it

is conceivable that TANs contribute to organising the pre-metastatic niche, as previously proposed for distant metastasis.[3,34] We thus extended our analysis to 175 non-metastatic TDLNs (NM-TDLNs, Supplementary table 1). Notably, we also observed nodal localisation of $CD66b^+$ TANs in a significant fraction of the NM-TDLNs (77/175, 44.0% $CI_{95\%}$ 36.5–51.7%). In terms of nodal localisation in NM-TDLNs, high $CD66b^+$ TAN density was found within the lymphatic sinuses (67/77, 87.0% $CI_{95\%}$ 77.4–93.6%; Supplementary figures 3 and 4). Also, within the nodal sinuses, $CD66b^+$ TANs co-existed with numerous $CD163^+$ macrophages and $CD3^+$ lymphocytes ($n = 5$; Supplementary figure 4h, i). These findings suggest that multiple interactions of TANs within the lymphatic sinuses might occur and may establish a pre-metastatic niche in TDLNs similar to distant sites.[35,36]

$CD66b^+$ TAN immune-contexture in squamous cell carcinoma of the oral cavity (OSCC)

In our screening cohort, $CD66b^+$ TAN infiltration in TDLNs was striking in head and neck squamous cell carcinoma (Figure 1a, Supplementary table 1). By co-culture experiments combining circulating neutrophils with three human OSCC lines, we found that OSCC cells provide a significant survival signal to neutrophils as measured by Vibrant dye assay (Figure 3a and Supplementary figure 6). A similar response, albeit attenuated, was seen with exposure of neutrophils to OSCC-derived supernatants (Figure 3b), which also induced neutrophil activation as revealed by membrane up-regulation of CD11b (Figure 3c) and down-regulation of CD62L (Figure 3d). By ELISA and blockade experiments, we found these effects were mostly dependent on GM-CSF, but not IL-6, released by OSCC cells (Figure 3b–e). To establish the clinical significance of $CD66b^+$ TAN infiltration, we measured $CD66b^+$ TAN density in a large retrospective cohort of OSCC ($n = 182$). We identified OSCC patients who underwent radical surgery of the PT with node dissection. Clinical details of the cohort are reported in Supplementary tables 2 and 4. A representative tissue block of the PT and at least one block containing multiple TDLNs were available for the analysis. For N^+ patients ($\geq$ Stage III AJCC), M-TDLNs were included (Supplementary figure 7). Data and representative images are shown in Figure 3, Supplementary figure 8 and Supplementary tables 2 and 3. In the PT, we analysed a mean tumor area of 105 ± 71 mm^2. The median density of $CD66b^+$ TANs was 175 cells mm^{-2}, and it was significantly higher in the invasive margin (IM) compared to the centre of the tumor (CT) (194 cells mm^{-2} vs 155 cells mm^{-2}; $P < 0.0001$; Supplementary table 4, Figure 3f).

We subsequently tested $CD66b^+$ TAN density in TDLNs by analysing M-TDLNs ($n = 219$), and NM-TDLNs ($n = 626$). For M-TDLNs, counts were also performed in the two distinct compartments, the metastatic nest ($M\text{-}TDLN^M$) and the surrounding nodal parenchyma ($M\text{-}TDLN^P$), the latter mainly accounting for $CD66b^+$ TANs within the lymphatic sinuses. TAN density in the PT showed a strong direct correlation with TAN density in TDLNs, particularly in the M-TDLNs ($r = 0.5$; $P < 0.001$; Figure 3g, Supplementary table 4). Remarkably, the strongest correlation between sub-regions was observed between the CT of the PT and the $M\text{-}TDLN^M$ (Spearman $r = 0.49$, $P < 0.001$; Figure 3g), consistent with CT $CD66b^+$ TANs receiving an appropriate imprinting signal(s) to establish a nodal pre-metastatic niche.

Clinical significance of TAN immune-contexture in OSCC compartments

Data on the prognostic significance of TAN density in human cancer are still inconclusive. We tested the clinical relevance of $CD66b^+$ TAN density in PTs and TDLNs. Univariate analysis of clinical-pathologic prognosticators for overall survival (OS) confirms that T stage, AJCC stage, nodal status and lympho-vascular invasion represented the strongest prognostic factors (Supplementary table 2). In particular and as previously recognised,[37] the occurrence of extracapsular spread (ECS) resulted in a striking decrease of survival estimates in patients with nodal metastasis. Moreover, the multivariable analysis confirmed nodal status as the most powerful independent prognosticator (Supplementary table 2). We then tested the prognostic significance of $CD66b^+$ TAN, as continuous variable, by performing a multivariable analysis including interaction terms in the model. Of note, when measured in the entire tumor area, the $CD66b^+$ TAN density was not significantly associated with prognosis. However, $CD66b^+$ TAN densities measured at the CT or at the IM were predictive of survival ($P = 0.019$ and $P = 0.033$,

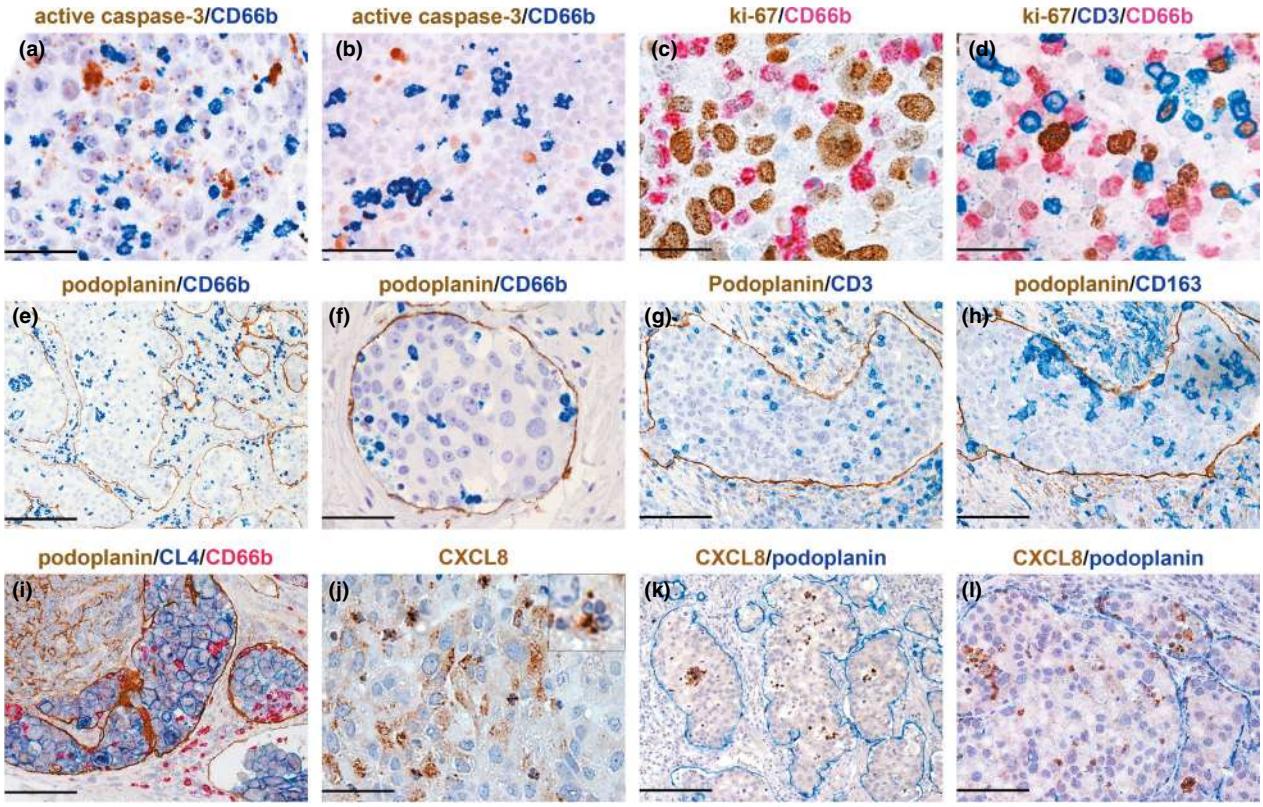

Figure 2. Lymphatic derivation of nodal CD66b$^+$ TANs. Sections of M-TDLNs **(a-d, i, l)** [from lung carcinoma **(a–d)** and gastric carcinoma **(i, l)**] and of PT **(e–h, j, k)** [from gastric **(e, f, k)** and lung **(g, h, j)** carcinomas] stained as labelled. As illustrated by double stain, most of CD66b$^+$ TANs from M-TDLNs are negative for active caspase-3 **(a, b)** and ki-67 **(c, d)** in both M-TDLN compartments (M-TDLN^M [**a**, **c**]; M-TDLN^P [**b**, **d**]). In primary carcinomas, CD66b$^+$ TANs are found within podoplanin$^+$ lymphatic vessels **(e, f)** similarly to CD3$^+$ T cells **(g)** and CD163$^+$ macrophages **(h)**, frequently admixed to carcinoma cells (**e**–**h**); this finding is confirmed in M-TDLN by a triple stain for podoplanin, CD66b and the carcinoma cell marker claudin 4 (CL4) **(i)**. Neoplastic cells **(j)** and TANs (inset in **j**, **k** and **l**) express CXCL8, also within lymphatic vessels **(k, l)**. The latter finding is observed in a primary gastric carcinoma **(k)** and in the corresponding M-TDLN **(l)**. Sections are counterstained with haematoxylin. Original magnification: 100× (**e**, **k**, scale bar 200 μm), 200× (**g**–**i**, **l**, scale bar 100 μm), 400× (**a**, **b**, **f**, **j**, scale bar 50 μm), 600× (**c**, **d** and inset in **j**, scale bar 33 μm).

respectively; Table 1). Moreover, a significant interaction of the variables was identified with the AJCC stage ($P = 0.013$ and $P = 0.013$, respectively; Table 1). Specifically, a higher CD66b$^+$ TAN density in the IM associated with worse prognosis in early stages I and II (H.R. 1.53, 0.87–2.71), whereas it predicted a better outcome in advanced stages III and IV (H.R. 0.42, 0.16–1.11; Figure 3h). By contrast, a higher CD66b$^+$ TAN density in the CT associated with worse prognosis in advanced stages III-IV (H.R. 1.59, 1.06–2.39) and with a better outcome in earlier stages I-II (H.R. 0.42, 0.16–1.11; Figure 3i and j).

Including M-TDLNs TAN densities, thus limiting the analysis to N$^+$ patients, a higher TAN density in the M-TDLN^M was associated with worse prognosis ($P = 0.004$; Figure 3k and l), suggesting a pro-tumor function of nodal TANs. The significant interaction detected between M-TDLNs TAN density and ECS status ($P = 0.036$) led to a stronger effect of the M-TDLNs TAN density on the outcome prediction in ECS positive patients (H.R. 2.19, 1.28–3.73) compared to ECS negative ones (1.22, 1.00–1.48; Table 1, Figure 3l).

We further extended these analyses on the clinical significance of CD66b$^+$ TAN^{Hi} in the TDLN^M by identifying the appropriate cut-off of TAN density at 163 cells mm^{-2} ($P = 0.07$). Of note, CD66b$^+$ TAN^{Hi} density in the M-TDLN^M confirms its detrimental effect in terms of 5 year-OS (14% $CI_{95\%}$ 4–52%, vs 49% $CI_{95\%}$ 37–63% Figure 3m). Moreover, when the ECS was considered, the M-TDLN^M CD66b$^+$ TAN^{Hi} / ECS$^+$ group showed the worst OS (2y-OS 17% $CI_{95\%}$ 3–99%, 5y-OS:

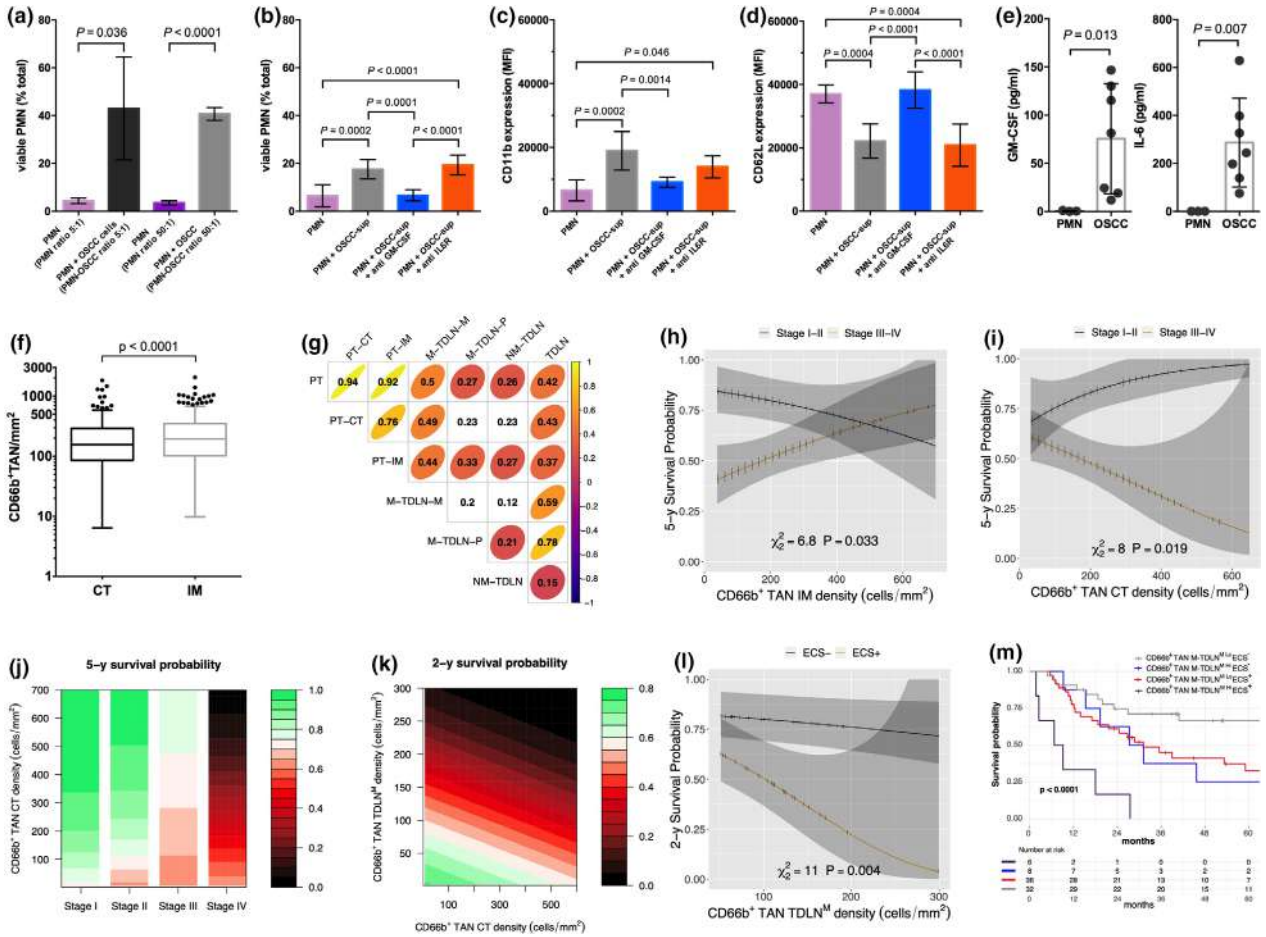

Figure 3. Clinical significance of CD66b$^+$ TANs in OSCC primary tumors (PTs) and TDLNs. Bar plots indicate the mean ± SD percentage of alive PMN after co-culture for 40 h with or without OSCC cell lines (SCC-4, $n = 3$; SCC-25, $n = 2$ or CAL-27, $n = 2$) **(a)**. PMN negative for vibrant staining were considered to be viable (see the Methods section); for conditioned media experiments, PMN were cultured for up to 40 h with or without OSCC-derived conditioned media (SCC-4 $n = 3$, SCC-25 $n = 3$ or CAL-27 $n = 3$) in the presence or absence of 10 μg mL^{-1} neutralising human anti-GM-CSF Ab or anti-IL-6R Ab **(b–d)**. In **b**, bar plots display the mean ± SD percentage of alive PMN at 40 h; in **c** and **d**, bar plots show the PMN mean ± SD fluorescence intensity (MFI) membrane expression of CD11b and CD62L, respectively, analysed at 20 h by flow cytometry; GM-CSF and IL-6 levels, as measured by ELISA, in cell-free supernatants collected from 2.5 × 10^6 mL^{-1} neutrophils and 5 × 10^4 mL^{-1} OSCC cell lines cultured for up to 40 h **(e)**; *P*-values were estimated by the one-way ANOVA followed by the Tukey's correction for pairwise comparisons **(a–d)** or by the unpaired *t*-test **(e)**. Boxplots of CD66b$^+$ TAN density in the OSCC PT compartments **(f)**; *P*-values were estimated by the Mann–Whitney *U*-test. Correlogram of CD66b$^+$ TAN density correlations among different tumor areas, r values are shown and ellipses show significant results ($P < 0.05$, Spearman test) **(g)**. Multivariable survival analysis (Overall Survival) graphs showing survival probability at 5 years according to Stage I and II or III and IV and CD66b$^+$ TAN density in the invasive margin (IM) **(h)** or in the centre of the tumor (CT) **(i)**. Heatmap showing the 5 years overall survival probability according to AJCC stage and CD66b$^+$ TAN density in the CT, adjusted for CD66b$^+$ TAN density in the IM **(j)**. Heatmap showing the 2 years overall survival probability according to CD66b$^+$ TAN density in the CT and CD66b$^+$ TAN density in M-TDLN^M, adjusted for ECS status **(k)**. Multivariable survival analysis (Overall Survival) graph showing survival probability at 2 years according to ECS status and CD66b$^+$ TAN density in M-TDLN^M **(l)**. Kaplan Meier curves of the univariate survival analysis according to the M-TDLN^M CD66b$^+$ TAN score (cut-off 163 cells mm^{-2}) showing subgroups of patients according to M-TDLN^M CD66b$^+$ TAN score and ECS status **(m)**, all pairwise comparisons (Holm adjusted) showed significant differences except between CD66b$^+$ TAN M-TDLN$^{M\ Hi}$ ECS$^-$ and CD66b$^+$ TAN M-TDLN$^{M\ Lo}$ ECS$^+$ ($P = 0.93$).

insufficient patients at risk) followed by the M-TDLN^M CD66b$^+$ TAN^{Hi}/ ECS$^-$ (5y-OS 25% CI$_{95\%}$ 8–83%) and M-TDLN^M CD66b$^+$ TAN^{Lo}/ECS$^+$ (33% CI$_{95\%}$ 19–55%) groups. The 5y-OS in the M-TDLN^M CD66b$^+$ TAN^{Lo}/ECS$^-$ reached 67% (CI$_{95\%}$ 52–86%; $P < 0.0001$) confirming the detrimental value of the high CD66b$^+$ TAN density in M-TDLNs (Figure 3k).

Table 1. Multivariable overall survival analysis of CD66b$^+$ TANs in OSCC primary tumors and TDLNs

Wald statistics				Effects	
Factor	Chi-square	d.f.	*P*	Factor	H.R. (95% C.I.)
Multivariable model 1					
AJCC stage	15.96	3	0.0012	AJCC stage (Stage III-IV : Stage I-II)	2.98 (1.6–5.55)
TAN density CT	7.98	2	0.0185	TAN density CT[a]	0.42 (0.16–1.11)
TAN density IM	6.84	2	0.0327	TAN density IM [a]	1.53 (0.87–2.71)
AJCC stage * TAN density CT	6.16	1	0.0130	TAN density CT[b]	1.59 (1.06–2.39)
AJCC stage * TAN density IM	6.06	1	0.0138	TAN density IM[b]	0.63 (0.42–0.96)
Multivariable model 2					
TAN density CT	0.72	1	0.3967	TAN density CT	1.27 (0.73–2.22)
TAN density IM	1.42	1	0.2327	TAN density IM	0.68 (0.36–1.29)
TAN density NM-TDLN	1.95	1	0.1624	TAN density NM-TDLN	1.3 (0.9–1.88)
TAN density M-TDLN^P	2.01	1	0.1561	TAN density M-TDLN^P	0.77 (0.53–1.11)
ECS	16.77	2	0.0002	ECS+ : ECS-[c]	2.48 (1.18–5.2)
TAN density M-TDLN^M	11.03	2	0.0040	TAN density M-TDLN^{Mc}	1.22 (1–1.48)
TAN density M-TDLN^M * ECS	4.41	1	0.0358	TAN density M-TDLN^{Md}	2.19 (1.28–3.73)

CT, centre of the tumor; C.I., confidence interval; d.f., degrees of freedom; ECS, extracapsular spread; H.R., hazard ratio; IM, invasive margin.
* Interaction.
[a]Adjusted to Stage I-II, TAN density CT = 155; TAN density IM = 194.
[b]Adjusted to Stage III-IV, TAN density CT = 155, TAN density IM = 194.
[c]Adjusted to ECS-, TAN density M-TDLN^M = 64.
[d]Adjusted to ECS+, TAN density M-TDLN^M = 64.

Stable TAN phenotype in OSCC compartments

The current understanding of markers uniquely associated with pro-tumor functions of human TANs is very limited. Our clinical data on OSCC highlight variability of TAN density in terms of prognostic significance, likely indicating the existence of stage or regional functional TAN subsets. We compared the expression of putative PMN-MDSC markers in various PT and TDLN compartments by using immunohistochemistry. In addition, a new specialised CD66b$^+$ TAN subset (referred as 'hybrid TANs') with anti-tumor capabilities and a mixed phenotype (additional expression of HLA-DR, CD14, CD206, CD86 and CCR7) was recently reported in the early-stage non-small-cell lung carcinoma.[14,38] We therefore tested also for the presence of this subset. These analyses were performed on TANs from PT early-stage OSCC cases with very good prognosis (for markers of hybrid TANs), PT late-stage OSCC with poor prognosis and their matched M-TDLNs (for putative PMN-MDSC markers). CD66b$^+$ TANs from PT early-stage OSCC cases with very good prognosis (n = 10) lacked nuclear morphology of hybrid TANs (round to oval), maintaining nuclear segmentation of canonical mature neutrophils as shown by DAPI stain (Figure 4a). In addition, by double staining, co-expression of HLADR, CD14 and CD66b was only limited to HLADR$^+$/CD14$^+$ macrophages phagocytosing CD66b$^+$ TANs (Figure 4b and c). Neutrophil phagocytosis was also confirmed by double staining of CD66b and CD163 and CD68 (Figure 4d and inset). In addition, TANs from late-stage OSCC PTs with poor prognosis and their matched M-TDLNs (Figure 4e–t) showed the same expression levels of putative PMN-MDSC markers[20,21] S100A9, arginase-1, c/EBPβ and pSTAT3 (n = 4). These markers were also observed in CD66b$^+$ neutrophils found in early-stage PTs and suppurative lymphadenitis (Figure 4h, l, p, t; n = 3).

Together, these findings indicate that novel biomarkers of clinical relevance are needed to identify TAN subsets with distinct biological properties.

CD66b$^+$ TANs in M-TDLNs interact with T cells

By using markers for lymphoid and dendritic cells, we next analysed cell interactions between CD66b$^+$ TANs and immune cells in a set of M-TDLNs (n = 9) positive for CD66b$^+$ TANs. CD66b$^+$ TANs frequently co-localise with CD3$^+$, CD8$^+$ T cells

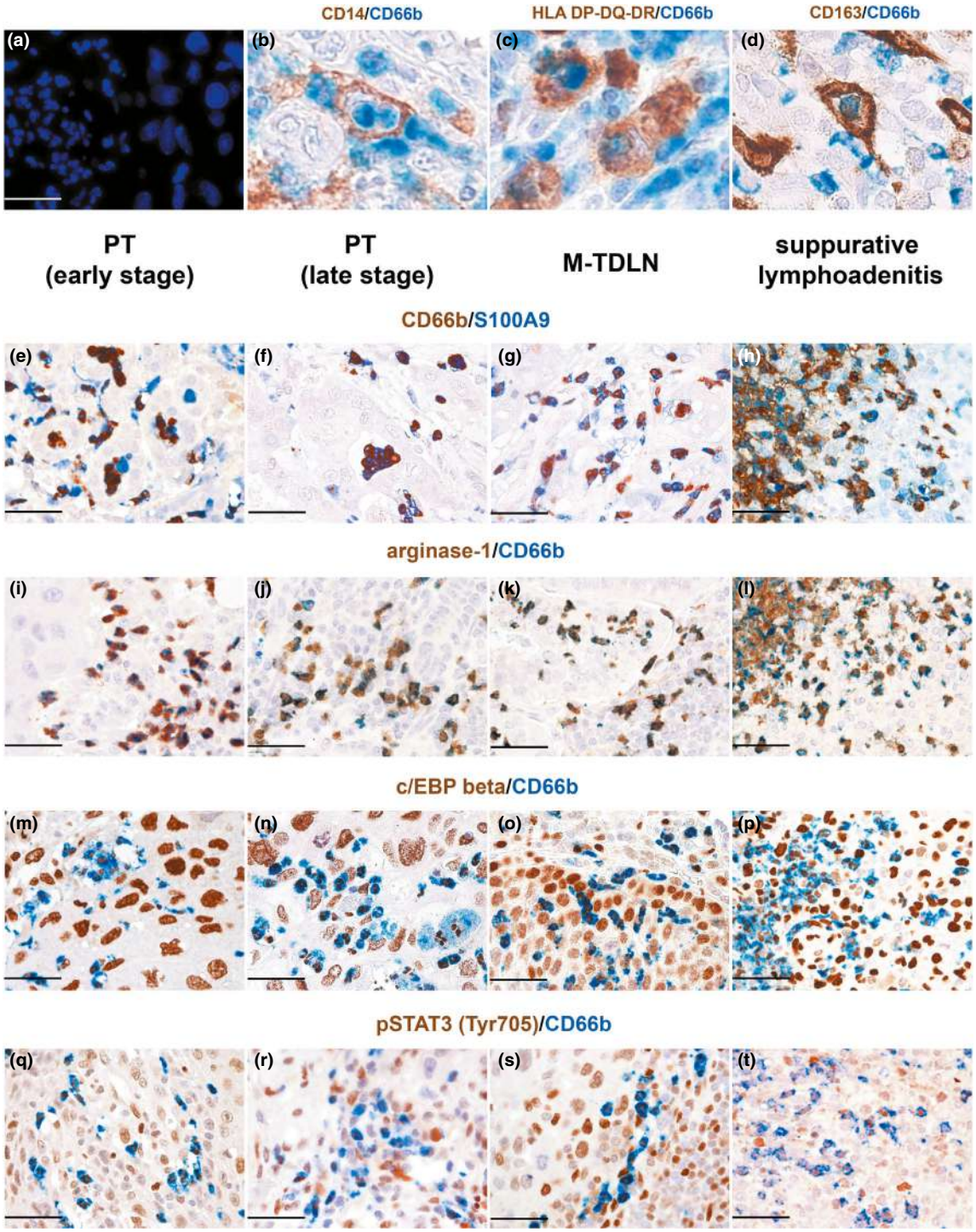

Figure 4. Analysis of the MDSC and hybrid TAN markers. Sections are from representative cases of primary tumors (PTs) and M-TDLNs at different disease stage, as labelled. DAPI highlighting TANs morphology and markers of hybrid TANs **(a–d)** and of MDSCs **(e–t)** are shown. The phenotype of neutrophils from suppurative lymphadenitis is shown as the control **(h, l, p, t)**. $CD66b^+$ TANs are negative of CD14 and HLA-DR; occasionally, they are found within the cytoplasm of $CD14^+$**(b)** and $HLA\text{-}DR^+$**(c)** cells, co-expressing the macrophage marker CD163 **(d)**. Sections are from early-stage OSCC PT (n = 2) **(a–e, i, m, q)** and late-stage PT from the stomach **(f)**, pancreas **(j)**, lung **(n)** and OSCC **(r)** coupled with their matched M-TDLNs **(g, k, o, s)**; a suppurative lymphadenitis case from non-tumor-bearing patients is included as control **(h, l, p, t)**. S100A9, c/EBPβ and pSTAT3 are also expressed on neoplastic cells and/or stromal cells. Sections are counterstained with haematoxylin. Original magnification: 400× (**e–t**, scale bar 50 μm); 600× (**a**, scale bar 33 μm). **b–d** are digitally resized to show phagocytosis.

and BDCA2$^+$ plasmacytoid dendritic cells (PDCs). While T cells are regularly found within the metastatic nest (M-TDLN^M) and in the surrounding nodal parenchyma (M-TDLN^P), PDCs are mainly restricted to the M-TDLN^P (Figure 5a). We expanded this observation by enumerating cell contacts between TANs and nodal CD3$^+$ T cells, using a recently designed image analysis algorithm[39] on double stained slides (see the Methods for details; $n = 9$). These data confirm that a significant fraction of CD66b$^+$ TANs contact T cells, particularly in the M-TDLN^P (Figure 5b and Supplementary figure 9a–d). Among T cells, a fraction of CD3$^+$ T cells interacting with CD66b$^+$ TANs express CD8 (Figure 5b and Supplementary figure 9e, f). We further explored TAN/T cell interaction and, by triple staining performed in M-TDLNs ($n = 3$), we detected conjugates of CD66b$^+$ TANs with CD3$^+$ T cells and S100$^+$ interdigitating dendritic cells (Figure 5c and d) in all cases. These findings indicate that functional interactions of TANs with T cells might occur also in M-TDLNs.

The occurrence of numerous cell contacts between CD66b$^+$ TANs and CD3$^+$ T cells in M-TDLNs (Figure 5b and Supplementary figure 9a, b) prompted us to investigate the T-cell status in M-TDLNs from the OSCC cohort. Most of T cells interacting with CD66b$^+$ TANs are negative for activated caspase-3 in both M-TDLN compartments (Supplementary figure 9c, d). We then tested the proliferation index (by ki-67 expression) of nodal T cells in M-TDLNs (Figure 5e–h). This analysis was performed in CD66b$^+$ TAN^{Lo} ($n = 10$) good prognosis and CD66b$^+$TAN^{Hi} ($n = 10$) worse prognosis tumor cases. Dermatopathic lymphadenitis (D-LD) ($n = 10$) samples served as a control group. We found that the proliferation index of CD3$^+$ T cells in the M-TDLN^M was significantly increased compare to M-TDLN^P and D-LD; of note, no differences were noted by sub-grouping for TAN density (Figure 5e). We then tested the T-regulatory phenotype using a triple staining for CD66b, Foxp3 and CD3 ($n = 10$) (Figure 5i–l). Again, the frequency of Foxp3$^+$CD3$^+$ regulatory T cells was increased in the M-TDLN^M compared to M-TDLN^P and D-LD; no significant differences were noted with respect to TAN density (Figure 5i). Sequential double staining for ki-67, CD3 and Foxp3 confirmed that the large majority (72.2%) of proliferating T cells in the M-TDLN^M corresponded to Foxp3 regulatory T cells (Figure 5m). In summary, these data suggest that the T-cell proliferation and polarisation towards a regulatory T-cell phenotype that dominates the M-TDLN^M compartment requires a complex modulation that is likely independent of TANs.

TAN signature in OSCC correlates with an EMT switch at the invasive margin of the PT

Our microscopic findings suggest that TANs directly interact with cancer cells within lymphatic vessels. Epithelial-to-mesenchymal transition (EMT) promotes epithelial tumor spread and recent observations suggest that neutrophils can efficiently escort tumor cells from blood vessels to metastatic tissues[40] and promote EMT.[41–43] Remarkably, the EMT signature is enriched in the basal and mesenchymal subtypes of OSCC, representing an independent predictor of nodal metastasis.[26,44] By analysing the TCGA-HNSC (The Cancer Genome Atlas-Head and Neck Squamous Cell Carcinoma) dataset containing 308 OSCC cases, we found that a partial EMT signature (Supplementary figure 10) correlates with a signature of genes highly expressed by neutrophils (Supplementary table 5). The neutrophil signature was obtained from previous studies[12,45,46] and validated using RNAseq analysis of highly pure peripheral blood neutrophils (not shown). Among top neutrophil-specific targets more associated with an EMT signature, we found TNFAIP6, MMP9, OLR1, MME, CXCR1, KCNJ15, TNFRSF10C, FCGRB3, CEACAM8 and FPR2 to be specific to PMNs,[10] Supplementary figure 11a and Supplementary table 6). Remarkably, this association was consistent for many of these targets also in early-stage OSCC (Supplementary figure 11b, c and Supplementary table 6). Of note, PMNs[10] were significantly enriched in basal and mesenchymal subtypes of OSCC (Figure 6a and b). Previous studies indicate a localisation of the p-EMT program to tumor cells found at the invasive margin (IM), indicating a contribution from the tumor microenvironment, likely driven by local availability of TGF-β from cancer associated fibroblasts.[26,47] Remarkably, TANs at the IM in OSCC also surround tumor areas showing an EMT switch and lymphangiogenesis. By triple staining, this observation was documented in a set of N$^+$ OSCC cases ($n = 10$) showing highly recurrent co-localisation of TANs with PDPN$^+$ki-67$^+$ proliferative lymphatics[48,49] around S100A9$^-$/PDPN$^+$ cancer cells (Figure 6c–f), a phenotype highly correlated with EMT.[26]

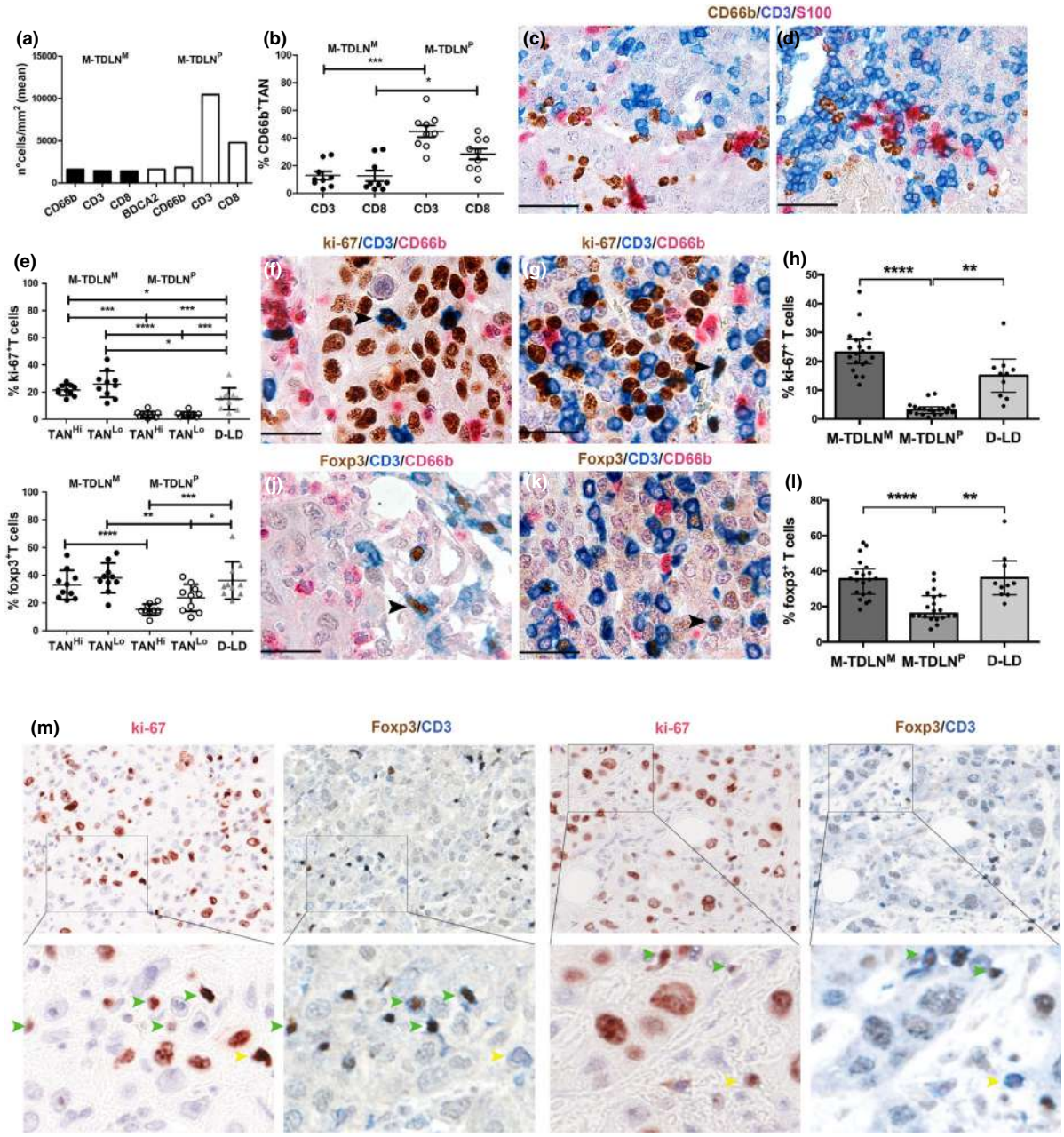

Figure 5. TAN/T-cell interactions and TANs polarisation in TDLNs. Graphs illustrate the frequency of different immune cell types **(a)** and the percentage of TANs interacting with T cells **(b)** in the metastatic nest (M-TDLN^{M}, black bars/circles) and nodal parenchyma (M-TDLN^{P}, white bars/circles) M-TDLN compartments quantified by using a digital microscopy algorithm by ImageJ software. Section of M-TDLN from gastric carcinoma illustrating a triple interaction between T cells, CD66b^{+} TANs and S100^{+} interdigitating dendritic cells **(c, d)** in M-TDLN^{M} (**c**) and M-TDLN^{P} **(d)** nodal compartments. The graphs illustrate the percentage of ki-67^{+}CD3^{+} proliferating T cells **(e)** and of foxp3^{+}CD3^{+} regulatory T cells **(h)** based on counts performed on triple stains **(f, g, j, k)**. The analysis has been performed in the metastatic nest (M-TDLN^{M}, black circles, **f, j**) and nodal parenchyma (M-TDLN^{P}, white circles, **g, k**) compartments of M-TDLNs CD66b^{+} TAN^{Hi} with worse prognosis (n = 10) compared with CD66b^{+}TAN^{Lo} with good prognosis (n = 10). As control group, dermatopathic lymphadenitis has been included (grey triangles, **d–l**). Boxplots reporting median and interquartile ranges of proliferating ki-67^{+} T cells (%, **h**) and of foxp3^{+} regulatory T cells (%) **(l)** in M-TDLN^{M}, M-TDLN^{P} or D-LD; P-values were estimated by the Kruskal–Wallis test and pairwise comparisons using the Dunn's procedure with a Bonferroni correction for multiple comparisons (*P < 0.05, **P < 0.01, ***P < 0.001, ****P < 0.0001). M-TDLNs shown are from OSCC cases (n = 4) **(f, g, j, k, m)** and stained as labelled. In **m**, images are taken as snapshot (from Aperio Scanscope) of digitalised slides and resized (bottom panels). Green arrow heads indicate ki-67^{+}CD3^{+}foxp3^{+} T cells, and yellow arrow heads indicate ki-67^{+}CD3^{+}foxp3^{-} T cells. Sections are counterstained with haematoxylin. Original magnification: 400× (**c**, **d,** scale bar 50 μm), 600× (**f**, **g**, **j**, **k**, scale bar 33 μm).

TAN modulate EMT signature in OSCC

We tested the hypotheses that this EMT-imprinting is acquired by circulating neutrophils from cancer patients. To this end, we prospectively collected peripheral blood from OSCC cases (n = 15) and matched controls (n = 13) and tested for the PMN[10] signature. The clinical and laboratory findings of this cohort are reported in Supplementary table 7 and Supplementary figure 12. Of relevance, the frequency of CD66b$^+$ neutrophils, most of which displayed a CD10$^+$ mature phenotype, as well as the neutrophil-to-lymphocyte ratio (NLR) were significantly increased in the OSCC group (Supplementary figure 12). The latter observations were consistent with our data collected from a larger patient cohort.[50] By phenotypic analysis of the circulating compartment of neutrophils, we could not detect significant differences for activation markers (CD62L, CD16, CD11b, CD54 or CD274), adhesion molecules (CD11c or CD11a) and chemotactic receptors, (CCR7, CXCR1, CXCR2 or C5aR), with the exception of a significantly increased expression of CXCR4 observed in the OSCC group (Supplementary figure 13). By reverse transcription quantitative PCR (RT-qPCR) analysis of the PMN[10] signature performed on total RNA extracted from circulating neutrophils, we could not detect significant differences between the OSCC and the control group. One exception was MME (alias CD10), that was significantly increased in the OSCC group (Figure 6g). These findings suggest that a full pro-EMT phenotype is likely acquired by local interaction of cancer cells with TANs.

DISCUSSION

By completing a large-scale analysis of human carcinoma samples, this study identified that CD66b$^+$ TANs recurrently colonise TDLNs, and that their high nodal density is associated with a detrimental prognosis in advanced stages squamous cell carcinomas (SCC). Based on direct and indirect evidence, we surmise that TANs in PTs and in TDLNs are major contributors in the organisation and evolution of the nodal metastatic niche, likely by modulating EMT. This hypothesis requires additional analysis using appropriate animal models for *in vivo* tracing and modulation of TAN functions. Importantly, lymph node metastasis can fuel distant metastasis in a significant fraction of cancers,[16,32] as also recently demonstrated by molecular analysis,[16] thus supporting an additional role of TANs in promoting systemic spread.

Similar to TANs in the PT, the TDLN cellular counterpart shows a segmented nuclear morphology and expresses a panel of neutrophil-specific molecules, including cytoplasmic granule-associated molecules and CD10, confirming their neutrophil identity and a mature phenotype.[51] In addition, at similar levels to the PT, the TANs in TDLNs express recently identified putative PMN-MDSC markers, including S100A9, arginase-1, pSTAT3 and c/EBPβ. It should be noted that this phenotype is observed also in neutrophils from suppurative lymphadenitis, indicating that co-expression of these markers by CD66b$^+$ cells is insufficient to define a TAN phenotype. In particular, a dense CD66b$^+$ TAN infiltration was identified in head and neck SCC, gastric and pancreatic adenocarcinoma and transitional bladder cancer. By contrast, breast carcinoma TDLNs are largely devoid of CD66b$^+$ TANs. In breast carcinoma, a lower CD66b$^+$ TAN density was also evident in the corresponding PT, suggesting site- and tumor-specific differences likely due to limited homing of the circulating TAN precursors from the blood.

An important and novel finding of this study is that CD66b$^+$ TANs in the PT form conjugates with cancer cells within lymphatic emboli. Accordingly, they reproduce similar conjugates in the marginal and intermediate sinuses of the corresponding TDLNs, within micro-metastatic foci. TAN entry into the TDLNs might occur via lymphatic vessels from the PT or, alternatively, through the blood circulation *via* high endothelial venules.[52] Our microscopic analysis supports the hypothesis that TANs could enter the TDLN via the lymphatic route with a potential role played by CXCL8, a chemokine known to regulate TAN recruitment and angiogenesis and supporting tumor progression.[33,53,54] CD66b$^+$ TANs are also found within sinuses of non-metastatic TDLNs (this study), suggesting that a steady lymphatic circulation of TANs might establish the pre-metastatic niche as observed in distant sites.[34,36,55] We hypothesise that TANs provide a survival signal to tumor cells or other cells (i.e. macrophages) co-existing in the nodal sinuses. Bidirectional signals between cancer cells and TANs might also result in the activation of TANs in proximity of tumor emboli.[56,57] TANs facilitate

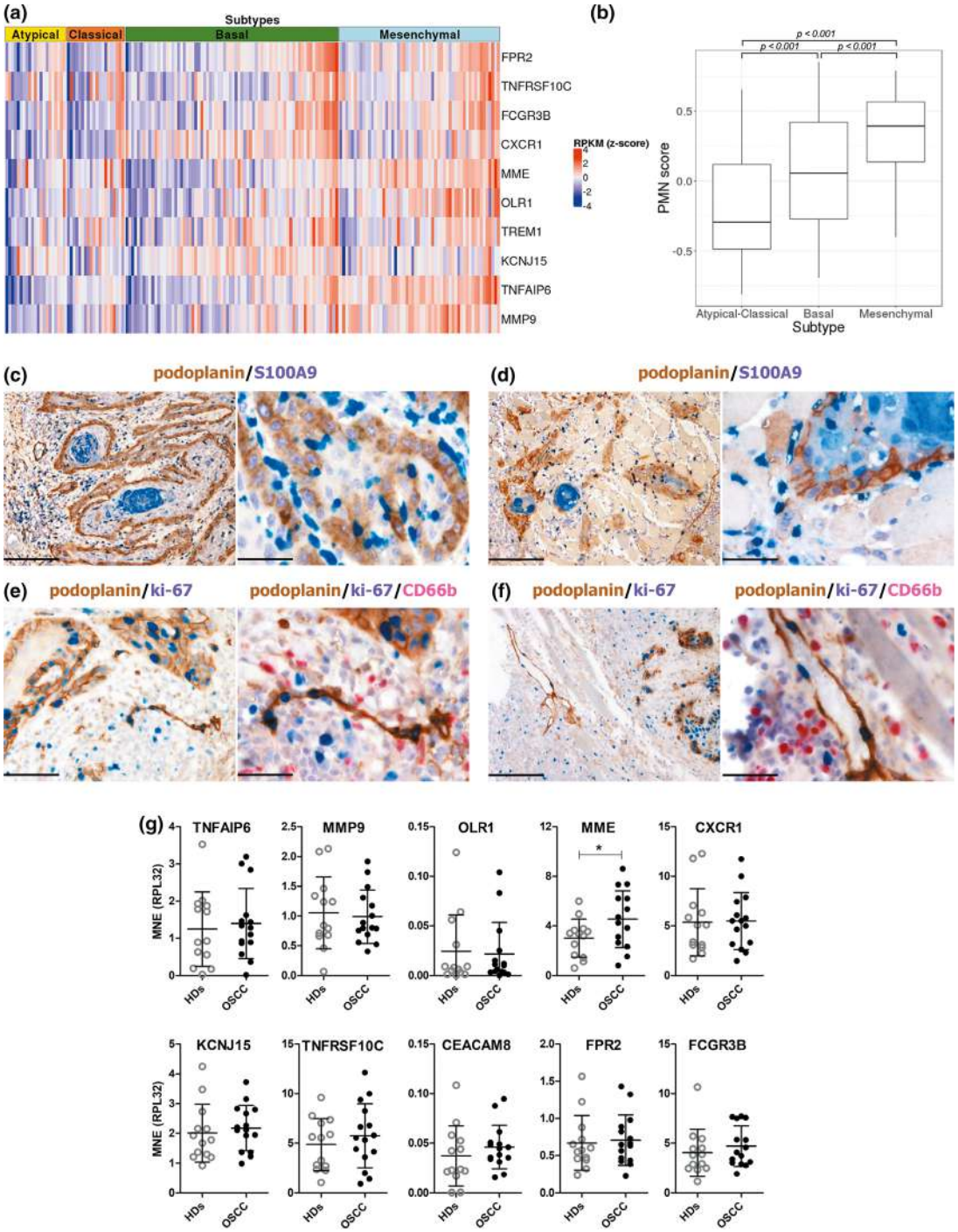

Figure 6. PMN signature in OSCC. **(a)** The heatmap shows the $\log_2$ RPKM values for the PMN signature genes grouped by Subtype annotation (n = 171 OSCC samples from the TCGA with available annotation). Samples are ordered in increasing overall expression values within Subtypes. **(b)** The boxplot of PMN score (computed using GSVA algorithm) separately for Subtype annotation. *P* values are estimated by a linear model and pairwise multiple comparisons adjusted for multiple tests with the Tukey–Kramer method. **(c–f)** Sections are from three OSCC PT (**d** and **f** single case) and stained as labelled. Sections are counterstained with haematoxylin. Original magnification: 100× (scale bar 200 μm; **c, d, f** images on the left), 200× (scale bar 100 μm; **e** image on the left) and 400× (scale bar 50 μm; **c–f** images on the right). **(g)** Dot plots show the mRNA expression of the PMN[10] in circulating neutrophils freshly isolated from HDs or OSCC patients, as evaluated by RT-qPCR. Gene expression is shown as mean normalised expression (MNE) units after RPL32 mRNA normalisation (mean ± SD). Each symbol stands for a single HD (open circle; n = 13) or OSCC patient (black circle; n = 15). *$P \leq 0.05$ by the unpaired t-test.

tumor cell migration, extravasation and subsequent invasion, thus fostering cancer cell arrest and growth at the metastatic site.[33] Notably, a set of proteases released by activated TANs has been implicated in the formation and dissemination of tumor aggregates in form of emboli.[58] These findings support the hypothesis that nodal TANs can promote cancer cell extravasation from the lymphatic sinuses, as well as their subsequent growth and invasion of the nodal parenchyma.[55] Since TAN density in the PT and in the M-TDLN^{M} is highly correlated, we surmise that only TANs receiving the appropriate imprinting signals in the PT can execute a pro-metastatic program in TDLNs.

Neutrophils are abundant in carcinomas showing squamous histology (SCC) mainly due to cancer cell intrinsic molecular traits such as SOX2 over-expression.[22–25] The latter occurs in SCC from various primary sites[59] including OSCC.[59–61] Moreover, TANs are known to foster squamous cell fate in murine models.[23] We found that OSCCs provide a significant survival and activation signal to TANs *via* GM-CSF expression. Mechanistically, the expression of a set of neutrophil genes is significantly associated with a partial EMT signature in OSCC. As recently proposed, EMT in cancer cells enhances their capacity to disseminate also *via* lymphatics,[62] which is highly relevant in terms of OSCC prognosis. Of note, EMT in OSCC represents an independent predictor of nodal metastasis and EMT-switched tumor cells localise to the IM, an area also enriched with lymphatic vessels.[26,44,48] We found that the top ten neutrophil-specific genes associated with the pro-EMT signature (referred as PMN[10]), are detected also in a subset of early-stage OSCC and are enriched in the basal and mesenchymal OSCC subtypes, typically associated with an EMT switch.[26,44] By the analysis of peripheral blood of OSCC patients, we also demonstrate that the expression of PMN[10] is very limited in circulating neutrophils, with only MME (alias CD10) being over-expressed. By contrast, over-expression of CXCR4, a chemokine receptor relevant in the neutrophil homeostasis,[63] in EMT of OSCC[64] and in neutrophil-mediated pro-metastatic function,[65] occurs early in circulating neutrophils from OSCC patients. Recent data on carcinomas from different sites have proposed TANs as a relevant player in promoting EMT.[41–43] Multiple findings from this study further strengthen this observation supporting that a full pro-EMT signature in OSCC is likely acquired at the TAN stage within the tumor tissue.

To establish the clinical relevance of nodal TAN infiltration, we performed a large-scale analysis of CD66b^{+} TAN density on a cohort of OSCC samples. In this cohort, high neutrophil count and NLR[50] were associated with poor prognosis. Data on the clinical relevance of CD66b^{+} TANs by IHC are partially conflicting, mainly due to differences in the analysis methods. However, recent computational approaches on a pan-cancer study revealed that TAN abundance represents a predictor of poor outcome.[12] To minimise the analytical biases in tissue monitoring, we strictly adhered to recently introduced guidelines.[66] We used a highly specific marker and measured a highly representative PT tissue area on whole digitalised slide (105 ± 71 mm^2). A significant interaction was observed between TAN density in the CT and in the IM and tumor Stage. A higher density in the CT was associated with worse prognosis only in advanced stage III and IV, whereas it predicted better prognosis in the earlier stages I and II; an opposite effect is observed for TAN density in the IM. Stage-dependent and spatially oriented molecular analysis of TAN are required to further expand our knowledge on this finding. However, this level of stage- and site-dependent functional heterogeneity requires further investigation. Among potential explanations, the existence of different TAN subsets, as recently described[67] supports the hypothesis of a dynamic change of pro-tumor TAN localisation along with disease progression. Among anti-tumor TANs, Eruslanov's groups have recently reported a specialised TAN subset with a hybrid phenotype found in early-stage non-small-cell lung cancer and associated with good prognosis.[14,38] As in other studies on human lymph nodes, these cells are found to express MHC-II molecules.[68] We could not identify a similar population in OSCC, likely indicating that hybrid anti-tumor TANs are primary site specific.

Our study identifies a contribution of nodal TANs in OSCC prognosis with a high TAN density in the metastatic nests (M-TDLN^{M}) predicting worse overall survival. This might indicate that nodal TANs can promote systemic spread, likely by immune escape. We found that TANs in TDLNs recurrently interact with T cells and interdigitating dendritic cells. Consistently, by image analysis we found that in M-TDLN, T-cell proliferation and polarisation towards a regulatory phenotype was significantly increased,

but not affected by a higher TAN density. Notably, we also found that TANs interact with nodal PDCs, a major source of type I IFN in human lymph nodes.[69] This finding might suggest that polarisation to N1 TANs via type I IFN[10] could occur[67] and likely be obtained by TLR8 or TLR9 agonists (Clinicaltrials.gov study identifiers: NCT02644967, NCT03445533, NCT03052205, NCT02521870, NCT03084640 and NCT0266877).

Overall, this study identifies and characterises the clinical relevance of a novel TAN compartment in carcinomas, particularly in SCC. Microscopic analysis and the clinical findings from the OSCC cohort highlight the relevance and the plasticity of TAN compartments in various disease stages and their role in promoting EMT. Tailored site and stage-dependent modulation of TANs from various compartments should be considered to be therapeutic option for carcinoma patients and in particular SCC.

METHODS

Tissues

This part of the study was approved by the local IRB to WV (WW-IMMUNOCANCER^{hum}, NP-906). Formalin-fixed paraffin embedded (FFPE) tissue blocks used for this study were retrieved from the tissue bank of the Department of Pathology (ASST Spedali Civili di Brescia, Brescia, Italy). Human tissues included human bone marrow, thymus, spleen, tonsil, lymph node, small bowel and appendix. In all, 278 metastatic (M-TDLNs) and 175 non-metastatic tumor-draining lymph nodes (NM-TDLNs), obtained from a total of 216 patients with primary carcinomas from different primary sites (skin, head and neck, thyroid, breast, lung, stomach, pancreas, colon, bladder and ovary) or cutaneous melanoma (17 cases). Details of M-TDLNs analysed are reported in Supplementary table 1. A total of 45 cases of primary melanoma (9 cases) and carcinoma from various sites were selected for a comparative analysis with M-TDLNs.

OSCC cohort

This part of the study was approved by the local IRB to WV (H&N Cancer, NP-2066). The retrospective study population included 182 histologically confirmed cases of oral cavity squamous cell cancer (OSCC) who underwent radical surgical resection and neck dissection between 2000 and 2014 (Otorhinolaryngology Department, ASST Spedali Civili di Brescia, Brescia, Italy). Patients with at least 12 months of follow-up or earlier death or recurrence were included. Salvage surgery, metastatic disease, immunological disorders or prior systemic treatment for malignancy represented exclusion criteria. Patients were regularly followed with clinical examinations and neck MRI or CT every 3–6 months. Details of the cohort are reported in Supplementary table 2. A prospective cohort, enrolled between June 2014 and December 2014, included patients affected by head and neck SCC, that underwent pre-treatment full blood collection for flow cytometry analysis and reverse transcription quantitative real-time PCR analysis; immunological disorders or prior systemic treatment for malignancy represented exclusion criteria.

Immunohistochemistry

Four-micron thick FFPE sections were used for immunohistochemical staining. The primary antibodies for this study are listed in the Supplementary table 8. The antibody used to detect granulocytes/TANs is CD66b diluted 1:200, clone G10F5, from BioLegend (San Diego, CA). The reaction was revealed by Novolink Polymer (Leica Microsystems, Wetzlar, Germany) followed by DAB. For double immunohistochemistry, after completing the first immune reaction, the second was visualised using Mach 4 MR-AP (Biocare Medical, Concord, CA), followed by Ferangi Blue (Biocare Medical) or New Fucsin (Agilent Technologies, Santa Clara, CA) as chromogen. For triple immunohistochemistry, after completing the second immune reaction, the third was visualised using a biotinylated system (Agilent) followed by AP-streptavidin and New Fucsin as chromogen. Sections were then counterstained with haematoxylin.

For the screening cohort, a training set of 15 cases on digitalised slides (IHC nuclear algorithm, Aperio Scanscope, Leica Microsystems) was used to define a three-tiered score for CD66b$^+$ TANs as it follows: S0 = $\leq$ 20 cell mm^{-2} (mean 12); S1 = $\leq$ 100 cells mm^{-2} (mean 59); S2 = > 100 cells mm^{-2} (mean 235). Neutrophils interactions with PDCs and T cells were analysed using a specifically designed algorithm in Image J by processing 10 captured high power field on CD66b/BDCA2, CD66b/CD3 and CD66b/CD8 double stained sections. Enumeration of proliferating (CD66b, CD3 and ki-67) and of regulatory (CD66b, CD3 and foxp3) T cells was performed by using ImageScope (Aperio Counter Tool) on triple stained sections of 20 M-TDLN cases from the OSCC cohort. Control cases were represented by six dermatopatic lymphadenitis.

For double sequential immunostains, the first reaction is deleted after first chromogen de-stain and stripping. Anti-ki-67 was used for the first immune reaction, revealed using Novolink Polymer and developed in 3-amino-9-ethylcarbazole chromogen (AEC), counterstained with haematoxylin and cover-slipped using gelatin. Subsequently, the slides were digitally scanned, using Aperio Scanscope CS (Leica Microsystems). After cover slip removal AEC was washed out and the slides were eluted using a 2-Mercaptoethanol/SDS solution (20 mL 10% w/v SDS with 12.5 mL 0.5 M Tris-HCl, pH6.8, 67.5 mL distilled water and 0.8 mL 2-ME). Slides were subsequently incubated in this solution in a water-bath pre-heated at 56°C for 30 min. Sections were washed for 1 h in distilled water. After unmasking in microwave, anti-foxp3 was revealed using Rat-on-Mouse HRP polymer (Biocare Medical) and 3.3′Diaminobenzidine. CD3 was revealed using Mach 4 MR-AP and Ferangi blue as chromogen and slides were counterstained with haematoxylin, cover-slipped and

digitally scanned. The two digital slides were processed using ImageScope. Slides were synchronised and corresponding tissue regions were analysed using the counter tool.

Immunoscore definition by image analysis

Stained slides were acquired using a ScanScope digital scanner. Images were viewed and organised using ImageScope software. Each scanned image was annotated manually and IHC Nuclear Image Analysis algorithm was chosen for the analysis. Areas of suppurative necrosis were excluded from the count. Data are expressed as number of $CD66b^+$ cells *per* mm^2. In the primary tumor (PT), immune cell density was measured either in the centre of the tumor (CT) and in the invasive margin (IM). The invasive margin was defined as the tissue area of 1 mm wide from the front of invasion of the tumor [700]. For the analysis of tumor-draining lymph nodes (TDLNs) at least one non-metastatic TDLN (NM-TDLN) was analysed; in N^+ patients, slides containing metastatic TDLN (M-TDLN) have been included. The density of $CD66b^+$TAN in M-TDLNs was counted in the metastatic nests ($M\text{-}TDLN^M$) and surrounding lymph node tissue ($M\text{-}TDLN^P$).

Isolation of neutrophils

Circulating neutrophils were isolated by density gradient centrifugation (Ficoll-Paque; GE Healthcare Life Sciences, Marlborough, MA) of whole blood collected in BD Vacutainer tubes with K_2EDTA (BD Biosciences, Franklin Lakes, NJ) from patients with OSCC or HDs or from buffy coats of healthy donors and further purified (approximately 99.7% purity) by negative selection using the EasySep neutrophil enrichment kit (StemCell Technologies, Vancouver, Canada) as previously described.[711] Human samples were obtained following informed, written, consent by healthy donors, in accordance with the Declaration of Helsinki. This study was carried out in accordance with the recommendations of Ethic Committee of the Azienda Ospedaliera Universitaria Integrata di Verona (Italy).

Cell cultures

Human oral squamous cell carcinoma (OSCC) cell lines, CAL-27 (DSMZ n° ACC 446), SCC-4 (DSMZ n° ACC 618), SCC-25 (DSMZ n° ACC 617), were purchased from Leibniz Institute DSMZ-German Collection of Microorganisms and Cell Cultures GmbH (DMSZ, Braunschweig, Germany). CAL-27 cell line was expanded in Dulbecco's modified Eagle medium (DMEM)(Corning, NY) at 37°C/5% CO_2, while SCC-25 and SCC-4 cell lines were expanded in DMEM:Ham's F12 (Euroclone, Pero, Milan, Italy) at a 1:1 ratio. All tissue culture media were supplemented with 10% FBS (< 0.5 EU per mL endotoxin, BioWhittaker-Lonza, Basel, Switzerland) and 1% of penicillin/streptomycin (pen/strep) (Corning).

Neutrophils co-culture with OSCC cell lines

Co-culture experiments were performed in 24-well culture plates (Corning) at 37°C/5% CO_2. Cell lines were plated at 5×10^4 mL^{-1} in RPMI (10% FBS, 1% P/S) 24 h prior the addition of neutrophils, to permit their adhesion to the plates. After the isolation, neutrophils were then suspended at 0.25 and 2.5×10^6 mL^{-1} in RPMI 1640 medium (Corning), containing 10% FBS and 1% of pen/strep and they were either plated alone, or directly added to the cell lines (at neutrophil:cell line ratios of 5:1 and 50:1), to be cultured for up to 40 h.

At the end of the incubation time, neutrophils were detached from the co-cultures by gently pipetting, then centrifuged at 300 × *g* for 5 min and finally suspended in 50 μL phosphate-buffered saline (PBS) at 1×10^6 mL^{-1} containing 2% FBS and 15 mm EDTA for flow cytometry assays.

Conditioned media experiments

Neutrophil were suspended in RPMI (10% FBS, 1% P/S) or conditioned media harvested from OSCC cell lines (CAL-27, SCC-4, SCC-25) plated at 5×10^6 mL^{-1} in 96-well culture plates (Corning) and then cultured for up to 40 h. Cytokine blocking experiments were conducted by culturing neutrophils in OSCC-derived conditioned media, previously pre-incubated for 30 min at 37°C in the presence of specific neutralising monoclonal antibodies (mAb) towards GM-CSF (10 μg mL^{-1}, R&D Systems, Minneapolis, MN). Alternatively, neutrophils were pre-incubated with IL-6R (10 μg mL^{-1} for 30 min, R&D Systems). After the incubation, neutrophils were then centrifuged at 300 × *g* for 5 min and finally suspended in 50 μL phosphatase-buffered saline (PBS) at 1×10^6 mL^{-1} containing 2% FBS and 2 mm EDTA for flow cytometry assays.

Flow cytometry

Neutrophils were incubated with 5% human serum (BioWhittaker-Lonza) for 5 min on ice and then stained for 30 min at 4°C using the following anti-human fluorochrome-conjugated mAbs or specific isotype controls listed in Supplementary table 8. For immunophenotypic characterisation of neutrophils from HD or OSCC patients, events were acquired on an eight-colour three-laser-MACSQuant Analyzer (Miltenyi Biotec, Bergish Gladbach, Germany) while for co-culture and conditioned media experiments, flow cytometry was performed by the use of a FACS MACSQuant Analyzer 16 Flow Cytometer (Miltenyi Biotec). Neutrophils were identified on the basis of their morphological parameters (forward scatter/side scatter) and the CD66b expression. Phenotypic analysis was performed on live cells, identified as Vybrant-negative (Vybrant® DyeCycle™ Violet; Life Technologies, Waltham, MA) or propidium iodide (Life Technologies) negative cells. Cell viability was defined as the percentage of cells that were negative for vibrant staining.

Data analysis was performed by using FlowJo software (Tree Star). The median fluorescence intensity (MFI) relative to each molecule was obtained by subtracting either the MFI of the correspondent isotype control or cell autofluorescence. Unpaired *t*-tests or one-way ANOVA analysis were performed, as appropriate.

Reverse transcription quantitative real-time PCR (RT-qPCR)

Immediately after purification, total RNA (0.1 μg) was extracted from 1×10^6 neutrophils by the RNeasy mini kit (Qiagen, Venlo, Limburg, The Netherlands) and reverse transcribed for RT-qPCR, performed as previously described,[722] utilising the gene-specific primer pairs (listed in Supplementary table 9), all purchased from Thermo Fisher Scientific). Data were calculated by Q-Gene software (http://www.gene-quantification.de/download.html) and expressed as mean normalised expression (MNE) units, after RPL32 normalisation.

Cytokines production

Cytokine concentrations in cell-free supernatants were measured by commercially available ELISA kits, specific for human IL-6 (Mabtech, Nacka Strand, Sweden) and GM-CSF (BioLegend). Detection limits of these ELISA were as follows: 10 pg mL^{-1} for IL-6 and 7.8 pg mL^{-1} for GM-CSF.

Data preprocessing and statistical analysis of the TCGA dataset

Raw counts for primary solid tumor samples were downloaded from GDC portal harmonised repository using TCGAbiolinks R/Bioconductor package ($n = 528$). FFPE samples were removed, and only samples corresponding to Oral Cavity anatomical area were kept ($n = 308$). Gene differential expression was tested, after library size normalisation based on TMM (the trimmed mean of M-values), using LIMMA linear modelling[733] function were used to model mean-variance relationship[744]. Single gene expression used as biomarker was computed as $\log_2$-RPKM. A global score for signature expression (either neutrophil or pEMT) was computed using single sample enrichment based on GSVA[755] algorithm: single sample enrichment score represents the degree to which the genes in a particular gene set are coordinately up- or down-regulated within a sample and were used as a global score for signature expression. Hierarchical clustering was performed using correlation based (Spearman) distance matrices and complete agglomeration method.

A filtering procedure to determine the PMN signature genes most associated with pEMT signature was performed based on two phases: first we performed a regularised Canonical Correlation Analysis (rCCA). This multivariate statistical procedure serves to identify linear combinations among variables between two datasets in order to maximise their correlation. The (two) new sets of canonical variates, constructed based on the original datasets, determine a pair of canonical variates with a maximised simple correlation. Each set of constructed canonical variates are uncorrelated with each other. Genes of both signatures are represented on a correlation circle plot where coordinates represent the correlation between each gene and the corresponding dimension. The correlation between genes in the two signatures can be visualised through the angles between two vectors (from the origin to the gene): if the angle is sharp, the correlation is positive, if the angle is obtuse the correlation is negative and if the angle is right the correlation is null. Therefore, PMN genes close to the bulk of pEMT genes and far from the origin are likely to be associated with the pEMT signature. In a second step we performed simple linear regression of pEMT score versus each PMN gene separately. PMN genes with a positive coefficient and significant *P*-value (not adjusted), were retained in the filtering procedure. This was performed for all samples and separately for low (I and II) and high (III and IV) stage.

Statistical analyses

Standard descriptive statistics were used for expressing means, standard deviations and CV. The Mann–Whitney *U*-test or the Kruskal–Wallis test was used for group comparisons, as appropriate. Differences in $CD66b^+$TAN density among different areas were analysed using nonparametric Spearman's rank correlation. For survival analysis, the overall survival (OS) was chosen as the end-point. Univariate survival curves were estimated using the Kaplan–Meier method and compared by the log-rank test. Cut-off in continuous predictors was estimated using maximally selected log-rank statistic. Multivariable analyses were performed using Cox proportional hazard models and expressed as hazard ratio (HR) with 95% confidence intervals (CI). To assess the clinical relevance of infiltrating $CD66b^+$ TANs in the PTs and lymph node areas, we modelled immune cells densities as continuous variables and their functional relationship with survival outcomes were evaluated investigating interactions with relevant clinical variables. In all the analysis, a significance level of 5% was used. GraphPad Prism Version 6.0 (San Diego, CA) and R (version 3.5.1) were used for statistical analysis.

ACKNOWLEDGMENTS

This work was supported by grants from Associazione Italiana per la Ricerca sul Cancro – Italy to WV (AIRC, IG-15378) and MAC (AIRC, IG-20339); we are grateful to Fondazione Beretta (Brescia, Italy) for support to SL and DB. We thank the pathologists (Drs Lucini, Battocchio and Ardighieri), technicians, clinicians, nurses and administrative employers who have provided support to the study and to the follow-up of OSCC patients. We are grateful to the Graphic Designer Matteo Vermi for help and supervision of the graphical abstract.

CONFLICTS OF INTEREST

The authors declare no competing financial interests.

AUTHOR CONTRIBUTION

William Vermi: Conceptualization; Formal analysis; Investigation; Supervision; Writing-original draft; Writing-review & editing. **Silvia Lonardi:** Conceptualization; Formal analysis; Methodology; Writing-original draft. **Francesco**

Missale: Conceptualization; Data curation; Formal analysis; Methodology; Software; Writing-original draft; Writing-review & editing. **Stefano Calza:** Data curation; Methodology; Software; Writing-original draft. **Mattia Bugatti:** Data curation; Formal analysis; Investigation; Methodology. **Raffaella Vescovi:** Data curation; Formal analysis; Methodology. **Debora Bresciani:** Data curation; Investigation. **Ravindra Uppaluri:** Conceptualization; Investigation; Writing-original draft. **Anne Egloff:** Data curation; Formal analysis. **Davide Mattavelli:** Data curation; Investigation. **Davide Lombardi:** Conceptualization; Data curation; Formal analysis; Investigation. **Luisa Benerini Gatta:** Methodology. **Olivia Marini:** Data curation; Investigation; Methodology. **Nicola Tamassia:** Data curation; Formal analysis; Investigation. **Elisa Gardiman:** Data curation; Formal analysis. **Marco Cassatella:** Conceptualization; Writing-original draft. **Patrizia Scapini:** Conceptualization; Data curation; Formal analysis; Investigation; Writing-original draft. **Piero Nicolai:** Resources.

REFERENCES

1. Mantovani A, Cassatella MA, Costantini C, Jaillon S. Neutrophils in the activation and regulation of innate and adaptive immunity. *Nat Rev Immunol* 2011; **11**: 519–531.
2. Mantovani A, Sozzani S, Locati M, Allavena P, Sica A. Macrophage polarization: tumor-associated macrophages as a paradigm for polarized M2 mononuclear phagocytes. *Trends Immunol* 2002; **23**: 549–555.
3. Talmadge JE, Gabrilovich DI. History of myeloid-derived suppressor cells. *Nature Rev Cancer* 2013; **13**: 739–752.
4. Jaillon S, Ponzetta A, Di Mitri D, Santoni A, Bonecchi R, Mantovani A. Neutrophil diversity and plasticity in tumour progression and therapy. *Nature Rev Cancer* 2020; **20**: 485–503.
5. Moses K, Brandau S. Human neutrophils: Their role in cancer and relation to myeloid-derived suppressor cells. *Semin Immunol* 2016; **28**: 187–196.
6. Scapini P, Marini O, Tecchio C, Cassatella MA. Human neutrophils in the saga of cellular heterogeneity: insights and open questions. *Immunol Rev* 2016; **273**: 48–60.
7. Bronte V, Brandau S, Chen S-H *et al*. Recommendations for myeloid-derived suppressor cell nomenclature and characterization standards. *Nat Commun* 2016; **7**: 12150.
8. Galdiero MR, Bonavita E, Barajon I, Garlanda C, Mantovani A, Jaillon S. Tumor associated macrophages and neutrophils in cancer. *Immunobiology* 2013; **218**: 1402–1410.
9. Fridlender ZG, Sun J, Kim S *et al*. Polarization of tumor-associated neutrophil phenotype by TGF-β: "N1" versus "N2" TAN. *Cancer Cell* 2009; **16**: 183–194.
10. Andzinski L, Kasnitz N, Stahnke S *et al*. Type I IFNs induce anti-tumor polarization of tumor associated neutrophils in mice and human. *Int J Cancer* 2016; **138**: 1982–1993.
11. Rotondo R, Barisione G, Mastracci L *et al*. IL-8 induces exocytosis of arginase 1 by neutrophil polymorphonuclears in nonsmall cell lung cancer. *Int J Cancer* 2009; **125**: 887–893.
12. Gentles AJ, Newman AM, Liu CL *et al*. The prognostic landscape of genes and infiltrating immune cells across human cancers. *Nat Med* 2015; **21**: 938–945.
13. Shen M, Hu P, Donskov F, Wang G, Liu Q, Du J. Tumor-associated neutrophils as a new prognostic factor in cancer: a systematic review and meta-analysis. *PLoS One* 2014; **9**: e98259.
14. Singhal S, Bhojnagarwala PS, O'Brien S *et al*. Origin and role of a subset of tumor-associated neutrophils with antigen-presenting cell features in early-stage human lung cancer. *Cancer Cell* 2016; **30**: 120–135.
15. Ponzetta A, Carriero R, Carnevale S *et al*. Neutrophils driving unconventional T cells mediate resistance against murine sarcomas and selected human tumors. *Cell* 2019; **178**: 346–360 e324.
16. Naxerova K, Reiter JG, Brachtel E *et al*. Origins of lymphatic and distant metastases in human colorectal cancer. *Science* 2017; **357**: 55–60.
17. Yang CW, Strong BS, Miller MJ, Unanue ER. Neutrophils influence the level of antigen presentation during the immune response to protein antigens in adjuvants. *J Immunol* 2010; **185**: 2927–2934.
18. Yang CW, Unanue ER. Neutrophils control the magnitude and spread of the immune response in a thromboxane A2-mediated process. *J Exp Med* 2013; **210**: 375–387.
19. Glodde N, Bald T, van den Boorn-Konijnenberg D *et al*. Reactive neutrophil responses dependent on the receptor tyrosine kinase c-MET limit cancer immunotherapy. *Immunity* 2017; **47**: 789–802 e789.
20. Ortiz ML, Lu L, Ramachandran I, Gabrilovich DI. Myeloid-derived suppressor cells in the development of lung cancer. *Cancer Immunol Res* 2014; **2**: 50–58.
21. McClure C, McPeak MB, Youssef D, Yao ZQ, McCall CE, El Gazzar M. Stat3 and C/EBPβ synergize to induce miR-21 and miR-181b expression during sepsis. *Immunol Cell Biol* 2017; **95**: 42–55.
22. Nagaraj AS, Lahtela J, Hemmes A *et al*. Cell of origin links histotype spectrum to immune microenvironment diversity in non-small-cell lung cancer driven by mutant kras and loss of Lkb1. *Cell Rep* 2017; **18**: 673–684.
23. Mollaoglu G, Jones A, Wait SJ *et al*. The lineage-defining transcription factors SOX2 and NKX2-1 determine lung cancer cell fate and shape the tumor immune microenvironment. *Immunity* 2018; **49**(764–779): e769.
24. Ferone G, Song JY, Sutherland KD *et al*. SOX2 is the determining oncogenic switch in promoting lung squamous cell carcinoma from different cells of origin. *Cancer Cell* 2016; **30**: 519–532.
25. Kargl J, Busch SE, Yang GH *et al*. Neutrophils dominate the immune cell composition in non-small cell lung cancer. *Nat Commun* 2017; **8**: 14381.
26. Puram SV, Tirosh I, Parikh AS *et al*. Single-cell transcriptomic analysis of primary and metastatic tumor ecosystems in head and neck cancer. *Cell* 2017; **171**: 1611–1624 e1624.
27. Vermi W, Micheletti A, Lonardi S *et al*. slanDCs selectively accumulate in carcinoma-draining lymph nodes and marginate metastatic cells. *Nature Commun* 2014; **5**: 3029.
28. Chtanova T, Schaeffer M, Han SJ *et al*. Dynamics of neutrophil migration in lymph nodes during infection. *Immunity* 2008; **29**: 487–496.

29. Hampton HR, Bailey J, Tomura M, Brink R, Chtanova T. Microbe-dependent lymphatic migration of neutrophils modulates lymphocyte proliferation in lymph nodes. *Nat Commun* 2015; **6**: 7139.
30. Giurisato E, Lonardi S, Telfer B *et al*. Extracellular-regulated protein kinase 5-mediated control of p21 expression promotes macrophage proliferation associated with tumor growth and metastasis. *Cancer Res* 2020; **80**: 3319–3330.
31. Rigby DA, Ferguson DJ, Johnson LA, Jackson DG. Neutrophils rapidly transit inflamed lymphatic vessel endothelium via integrin-dependent proteolysis and lipoxin-induced junctional retraction. *J Leukoc Biol* 2015; **98**: 897–912.
32. De Larco JE, Wuertz BR, Furcht LT. The potential role of neutrophils in promoting the metastatic phenotype of tumors releasing interleukin-8. *Clin Cancer Res* 2004; **10**: 4895–4900.
33. Chen MB, Hajal C, Benjamin DC *et al*. Inflamed neutrophils sequestered at entrapped tumor cells via chemotactic confinement promote tumor cell extravasation. *Proc Natl Acad Sci USA* 2018; **115**: 7022–7027.
34. Wculek SK, Malanchi I. Neutrophils support lung colonization of metastasis-initiating breast cancer cells. *Nature* 2015; **528**: 413–417.
35. Kaplan RN, Rafii S, Lyden D. Preparing the "soil": the premetastatic niche. *Cancer Res* 2006; **66**: 11089–11093.
36. Psaila B, Lyden D. The metastatic niche: adapting the foreign soil. *Nature Rev Cancer* 2009; **9**: 285–293.
37. Ferlito A, Rinaldo A, Devaney KO *et al*. Prognostic significance of microscopic and macroscopic extracapsular spread from metastatic tumor in the cervical lymph nodes. *Oral Oncol* 2002; **38**: 747–751.
38. Mishalian I, Bayuh R, Eruslanov E *et al*. Neutrophils recruit regulatory T-cells into tumors via secretion of CCL17–a new mechanism of impaired antitumor immunity. *Int J Cancer* 2014; **135**: 1178–1186.
39. Vescovi R, Monti M, Moratto D *et al*. Collapse of the plasmacytoid dendritic cell compartment in advanced cutaneous melanomas by components of the tumor cell secretome. *Cancer Immunol Res* 2019; **7**: 12–28.
40. Szczerba BM, Castro-Giner F, Vetter M *et al*. Neutrophils escort circulating tumour cells to enable cell cycle progression. *Nature* 2019; **566**: 553–557.
41. Kalluri R, Weinberg RA. The basics of epithelial-mesenchymal transition. *J Clinical Invest* 2009; **119**: 1420–1428.
42. Zhang W, Gu J, Chen J *et al*. Interaction with neutrophils promotes gastric cancer cell migration and invasion by inducing epithelial-mesenchymal transition. *Oncol Rep* 2017; **38**: 2959–2966.
43. Wang Y, Chen J, Yang L *et al*. Tumor-contacted neutrophils promote metastasis by a CD90-TIMP-1 juxtacrine-paracrine loop. *Clin Cancer Res* 2019; **25**: 1957–1969.
44. Puram SV, Parikh AS, Tirosh I. Single cell RNA-seq highlights a role for a partial EMT in head and neck cancer. *Mol Cell Oncol* 2018; **5**: e1448244.
45. Abbas AR, Baldwin D, Ma Y *et al*. Immune response in silico (IRIS): immune-specific genes identified from a compendium of microarray expression data. *Genes Immun* 2005; **6**: 319–331.
46. Veglia F, Perego M, Gabrilovich D. Myeloid-derived suppressor cells coming of age. *Nat Immunol* 2018; **19**: 108–119.
47. Natsuizaka M, Whelan KA, Kagawa S *et al*. Interplay between Notch1 and Notch3 promotes EMT and tumor initiation in squamous cell carcinoma. *Nature Commun* 2017; **8**: 1758.
48. Agarwal D, Pardhe N, Bajpai M *et al*. Characterization, localization and patterning of lymphatics and blood vessels in oral squamous cell carcinoma: a comparative study using D2–40 and CD-34 IHC marker. *J Clin Diagnostic Res* 2014; **8**: Zc86-89.
49. Balsat C, Signolle N, Goffin F *et al*. Improved computer-assisted analysis of the global lymphatic network in human cervical tissues. *Mod Pathol* 2014; **27**: 887–898.
50. Mattavelli D, Lombardi D, Missale F *et al*. Prognostic nomograms in oral squamous cell carcinoma: the negative impact of low neutrophil to lymphocyte ratio. *Front Oncol* 2019; **9**: 339.
51. Marini O, Costa S, Bevilacqua D *et al*. Mature CD10+ and immature CD10- neutrophils present in G-CSF-treated donors display opposite effects on T cells. *Blood* 2017; **129**: 1343–1356.
52. Leliefeld PH, Koenderman L, Pillay J. How neutrophils shape adaptive immune responses. *Front Immunol* 2015; **6**: 471.
53. Krzystek-Korpacka M, Matusiewicz M, Diakowska D *et al*. Elevation of circulating interleukin-8 is related to lymph node and distant metastases in esophageal squamous cell carcinomas-implication for clinical evaluation of cancer patient. *Cytokine* 2008; **41**: 232–239.
54. Chalivendra V, Kanchi KL, Onken MD, Winkler AE, Mardis E, Uppaluri R. Genomic analysis to define molecular basis of aggressiveness in a mouse model of oral cancer. *Genom Data* 2015; **3**: 61–62.
55. Sionov RV, Fridlender ZG, Granot Z. The multifaceted roles neutrophils play in the tumor microenvironment. *Cancer Microenviron* 2015; **8**: 125–158.
56. Kamioka Y, Takakura K, Sumiyama K, Matsuda M. Intravital Forster resonance energy transfer imaging reveals osteopontin-mediated polymorphonuclear leukocyte activation by tumor cell emboli. *Cancer Sci* 2017; **108**: 226–235.
57. Fidler IJ, Gersten DM, Hart IR. The biology of cancer invasion and metastasis. *Adv Cancer Res* 1978; **28**: 149–250.
58. Yui S, Tomita K, Kudo T, Ando S, Yamazaki M. Induction of multicellular 3-D spheroids of MCF-7 breast carcinoma cells by neutrophil-derived cathepsin G and elastase. *Cancer Sci* 2005; **96**: 560–570.
59. Ren ZH, Zhang CP, Ji T. Expression of SOX2 in oral squamous cell carcinoma and the association with lymph node metastasis. *Oncol Lett* 2016; **11**: 1973–1979.
60. Chou MY, Hu FW, Yu CH, Yu CC. Sox2 expression involvement in the oncogenicity and radiochemoresistance of oral cancer stem cells. *Oral Oncol* 2015; **51**: 31–39.
61. Liang X, Deng M, Zhang C *et al*. Combined class I histone deacetylase and mTORC1/C2 inhibition suppresses the initiation and recurrence of oral squamous cell carcinomas by repressing SOX2. *Cancer Lett* 2019; **454**: 108–119.

62. Pang M-F, Georgoudaki A-M, Lambut L *et al*. TGF-β1-induced EMT promotes targeted migration of breast cancer cells through the lymphatic system by the activation of CCR7/CCL21-mediated chemotaxis. *Oncogene* 2016; **35**: 748–760.
63. Devi S, Wang Y, Chew WK *et al*. Neutrophil mobilization via plerixafor-mediated CXCR4 inhibition arises from lung demargination and blockade of neutrophil homing to the bone marrow. *J Exp Med* 2013; **210**: 2321–2336.
64. Duan Y, Zhang S, Wang L *et al*. Targeted silencing of CXCR4 inhibits epithelial-mesenchymal transition in oral squamous cell carcinoma. *Oncol Lett* 2016; **12**: 2055–2061.
65. Tulotta C, Stefanescu C, Chen Q, Torraca V, Meijer AH, Snaar-Jagalska BE. CXCR4 signaling regulates metastatic onset by controlling neutrophil motility and response to malignant cells. *Sci Rep* 2019; **9**: 2399.
66. Galon J, Mlecnik B, Bindea G *et al*. Towards the introduction of the 'Immunoscore' in the classification of malignant tumours. *J Pathol* 2014; **232**: 199–209.
67. Zilionis R, Engblom C, Pfirschke C *et al*. Single-cell transcriptomics of human and mouse lung cancers reveals conserved myeloid populations across individuals and species. *Immunity* 2019; **50**: 1317–1334.e10.
68. Lok LSC, Dennison TW, Mahbubani KM, Saeb-Parsy K, Chilvers ER, Clatworthy MR. Phenotypically distinct neutrophils patrol uninfected human and mouse lymph nodes. *Proc Natl Acad Sci USA* 2019; **116**: 19083–19089.
69. Cella M, Jarrossay D, Facchetti F *et al*. Plasmacytoid monocytes migrate to inflamed lymph nodes and produce large amounts of type I interferon. *Nat Med* 1999; **5**: 919–923.
70. Galon J, Pages F, Marincola FM *et al*. Cancer classification using the Immunoscore: a worldwide task force. *J Transl Med* 2012; **10**: 205.
71. Calzetti F, Tamassia N, Arruda-Silva F, Gasperini S, Cassatella MA. The importance of being "pure" neutrophils. *J Allergy Clin Immunol* 2017; **139**: 352–355.e356
72. Arruda-Silva F, Bianchetto-Aguilera F, Gasperini S *et al*. Human neutrophils produce CCL23 in response to various TLR-Agonists and TNFα. *Front Cell Infect Microbiol* 2017; **7**: 176.
73. Ritchie ME, Phipson B, Wu D *et al*. limma powers differential expression analyses for RNA-sequencing and microarray studies. *Nucleic Acids Res* 2015; **43**: e47.
74. Law CW, Chen Y, Shi W, Smyth GK. voom: precision weights unlock linear model analysis tools for RNA-seq read counts. *Genome Biol* 2014; **15**: R29.
75. Hanzelmann S, Castelo R, Guinney J. GSVA: gene set variation analysis for microarray and RNA-seq data. *BMC Bioinformatics* 2013; **14**: 7.

Supporting Information

Additional supporting information may be found online in the Supporting Information section at the end of the article.